Design of a Horizontal Axis Open-Centre Tidal Stream Turbine using Computational Fluid Dynamics

Amy-Lee Gunter

A Thesis

in

The Department of Mechanical and Industrial Engineering

Presented in Partial Fulfillment of the Requirements

For the Degree of Master of Applied Science in Mechanical Engineering

Concordia University

Montreal, Quebec, Canada

December 2015

CONCORDIA UNIVERSITY
School of Graduate Studies

This is to certify that the thesis prepared

By: Amy-Lee Gunter

Entitled: Design of a Horizontal Axis Open-Centre Tidal Stream Turbine using Computational Fluid Dynamics

and submitted in partial fulfillment of the requirements for the degree of

Master of Applied Science (Mechanical Engineering)

complies with the regulations of the University and meets the accepted standards with respect to originality and quality.

Signed by the final Examining Committee:

_____ Chair
Dr. Gerard J. Gouw

_____ Examiner
Dr. Hua Ge

_____ Examiner
Dr. Charles Basenga Kiyanda

_____ Supervisor
Dr. Hoi Dick Ng

_____ Supervisor
Dr. Lyes Kadem

Approved by _____

Dr. Ali Dolatabadi,
Graduate Program Director

December 22, 2015 _____

Dr. Amir Asif, Dean
Faculty of Engineering and Computer Science

Abstract

Design of a Horizontal Axis Open-Centre Tidal Stream Turbine using Computational Fluid Dynamics

Amy-Lee Gunter

Tidal energy is one of the most promising emerging renewable energy sources which remains largely untapped, due primarily to the challenges of submerged operation within sensitive marine environments. Extracting kinetic energy from dense and energetic flow streams which vary in height, reverse flow direction roughly twice a day and carry sediment as well as marine life requires a unique application of engineering knowledge. A variety of tidal turbine technologies have been developed in response, although as yet the industry is far from mature and there remains great potential for improvement. The research presented in this study introduces a new type of turbine design which has been developed specifically to address the issue of balancing marine friendly technology with efficient energy harvest. This is accomplished through the use of an open-centre concept which houses the blades between the hub and shroud, thus minimizing the risk of blade tip impact and providing free passage through the central aperture.

In this study several iterations of the design are tested using the methods of computational fluid dynamics (CFD), each one featuring a different helical blade geometry of varying length and twist angle. A numerical model of the new design is presented in which the energy generation potential is assessed by measuring the amount of torque produced by a stationary blade placed in a steady flow. The torque is calculated by determining the pressure force acting on each blade surface and the resulting moment generated about the rotation axis of the turbine. This method allows for a great number of geometries to be tested under simulated turbine operating conditions, without requiring a prohibitive amount of computational resources. The initial assessment of this new type of turbine is promising, indicating that certain blade geometries produce a greater amount of torque than a model of the conventional open-centre turbine developed by OpenHydro.

Acknowledgements

I would like to thank Dr. Hoi Dick Ng and Dr. Lyes Kadem for their excellent advice and guidance throughout my academic career, providing encouragement and support in abundance. From my first endeavours in the lab as an undergraduate, to preparing me for what is now becoming a most rewarding research career, they have been instrumental in my success.

I am also grateful to have colleagues in the laboratory who so generously devoted their own time and energy to helping me with my research. It was through many animated discussions with Rocco Portaro that this research finally took shape, and so I would like to thank him for his patience and determination.

Finally I would like to thank my family, who have listened to my ideas and provided invaluable insight into all aspects of this research. Their encouragement kept me focused, the free meals kept me fed, and their limitless optimism kept me working hard all the way to the end.

Table of Contents

List of Figures

List of Tables

Nomenclature

List of Symbols

A	swept area	[m^2]
A_c	cell area	[m^2]
C_μ	$k-\epsilon$ model constant	[-]
C_T	total torque coefficient	[-]
d	perpendicular distance from axis of rotation	[m]
F	force exerted	[N]
F_p	pressure force	[N]
F_{p_c}	perpendicular pressure force acting on the cell surface	[N]
F_{p_t}	tangential pressure force acting on the cell surface	[N]
k	turbulent kinetic energy	[kj/kg]
L	characteristic length of the flow	[m]
L	scale of the largest eddies in turbulent flow	[m]
l_b	blade length	[m]
l_p	helix pitch	[m]
l_r	cell radial distance	[m]
M_T	total torque	[N·m]
M_{T_c}	total torque produced by cell	[N·m]
M_{T_r}	total torque produced by full rotor	[N·m]
P_T	total pressure	[Pa]
p	pressure	[Pa]
R	rotor radius	[m]
Re	Reynolds Number	[-]
r	hub radius	[m]
t	time	[s]
U	mean flow velocity	[m/s]
V	free stream velocity	[m/s]

u_i	i-th component of velocity	[m/s]
x_i	i-th space dimension	[m]

Greek Symbols

ϵ	turbulence dissipation rate	[m^2/s^3]
μ_t	turbulent eddy viscosity	[m^2/s]
η	smallest length scale in turbulent flow	[m]
ρ	density	[kg/m^3]
ν	kinematic viscosity	[m^2/s]
ν_t	turbulent kinematic viscosity	[m^2/s]
τ_{ij}	Reynolds stresses	[m^2/s^2]
ω	specific turbulence dissipation rate	[s^{-1}]
Ω	absolute value of vorticity	[s^{-1}]
φ	helix angle	[deg]
α	blade twist angle	[deg]

Chapter 1

1. Introduction

This chapter introduces the present research by giving a brief overview of the renewable energy industry in general, with a greater focus on tidal energy and the challenges associated with its exploration. The current state of tidal stream technology is presented, as well as some of the more innovative concepts being developed by the industry. Finally, a new type of tidal stream turbine is introduced, with an explanation of the novel features which distinguish it from conventional tidal turbine designs.

1.1 Renewable Energy Industry

For some time now the renewable energy sector has been the focus of a significant amount of research effort, and as such has enjoyed a rapid increase in both the diversity and efficacy of the related technology. Efforts to identify new sources of renewables have produced a wealth of options, which are as diverse as they are practical. There are however just a few major players when it comes to large scale commercial electricity generation, and these include solar power, wind energy and various forms of ocean energy. The oceans are undeniably our most untapped resource, containing an immense amount of potential in the form of wave, thermal and tidal energy. The European Ocean Energy Association (EOEA) estimated that 0.1% of the ocean's kinetic energy could satisfy the world's current energy requirements five times over, highlighting the need to further develop ocean energy technology (EOEA, 2009).

The potential of any renewable energy source can be assessed based on a few key criteria. Ease of access is of course of prime importance, and in this respect solar and wind energy are highly ranked. The ease with which it can be efficiently converted into useful energy is also critical, a point which is demonstrated by the frustrating absence of fusion reactors in our energy sector. The amount of energy available for conversion is a serious consideration as well, and again an area in which solar, wind and ocean energy all score very well. Once the electricity has been generated it needs to be introduced to the grid, therefore easy access to an entry point is crucial. For example, offshore wind farms struggle to balance wind-rich locations with grid access, and so additional infrastructure is often required. Structures which house the generators, and any other necessary technology, should also be easily accessible in order to facilitate construction and maintenance. Harnessing renewables is of course part of a larger mission to protect the planet and its varied ecosystems. Therefore ensuring that the development of any renewable resource aligns with that mandate, and does not adversely affect

the environment, is inherently part of the assessment. This point is illustrated by the highly controversial topic of hydroelectric dams, which in their construction often flood vast regions with devastating effects on wildlife and their habitats.

Wind and solar power are well-established industries and ocean energy is rapidly joining the ranks, although it has been somewhat slow out of the gates. The oceans contain a massive amount of potential in the form of kinetic, thermal and chemical energy. However harnessing this energy presents a few unique challenges, and it is only recently that we have developed the technology to overcome some of those hurdles. Although the off shore oil and gas industry is now considered by many to be the root of all evil with respect to the health of our planet, it has also sponsored the development of crucial underwater construction technology and corrosion resistant materials which now play an important role in the ocean renewables industry (Lewis et al., 2011). It is undoubtedly in large part due to these advances in marine environment technology that ocean energy is now taking the reins and surging into the forefront of the renewable energy industry.

1.2 Tidal Energy

Ocean energy can be divided into four main categories, namely wave, tidal and ocean currents, thermal energy conversion and salinity gradients. All ocean energy technologies are in the pre-commercial research and development stages, with the exception of tidal barrages, which will be discussed below. The benefits of ocean energy include a relatively high energy density and an over-abundance of prime locations for energy extraction and conversion. Tidal energy in particular offers the added bonus of perfect flow predictability and consistency, two areas in which wind energy struggles. Tidal streams are generated by the flow of water between high and low tide, the precise timing of which can be predicted and is not influenced by weather or seasonal changes. The flow speed of tidal streams is a function of seabed bathymetry and global ocean current behaviour, and therefore with the right combination of these two factors it is possible to generate relatively fast flow speeds. Prime locations of this sort occur near shorelines around the globe, providing ample opportunity for many countries to leverage tidal energy. The inherent proximity of strong tidal currents to land is an important factor, which places it at the top of the list of ocean energy resources, above wave and thermal gradients. Although all ocean energy technologies are still in the early stages of development and their impact on the environment is still somewhat unknown, initial assessments from monitoring programs indicate that their influence remains low (Keenan et al., 2011).

Tidal energy has actually been harvested for over 40 years through the use of dam-like structures called barrages, however this approach is no longer considered sustainable owing to the detrimental effect on the surrounding marine environment (Lloyd-Evans, 2005). Tidal barrages use the change in water height between low and high tide to drive turbines housed in the dam wall, thus converting potential energy into electricity. As is often the case with hydroelectric dams, the artificial manipulation of water levels and flow behaviour is rarely of benefit to the surrounding wildlife. This type of interference results in habitat flooding and inhibits the movement of marine life. As a result, the tidal energy industry has begun to shy away from plans for future tidal barrage development (Polagye et al., 2010). Of course the alternative to using barrages is to instead directly use the kinetic energy of the stream as it flows from high to low tide, thus eliminating the need for a dam altogether. This is accomplished through the use of tidal stream turbines (TST), which essentially convert the kinetic energy of the tidal stream into electricity using similar generators to those found in wind turbines. There are currently only a few types of TSTs in commercial operation, with several more in the research and development pipeline.

1.2.1 Tidal Challenges

Despite the aforementioned benefits of tidal energy, there are in fact several reasons why it remains vastly untapped, not the least of which involve operating in a submerged saline environment while subject to enormous structural stresses. Operating much like a wind turbine underwater, the TST must however be able to withstand the force of a very dense and energetic flow. In addition, any TST design must be able to make use of dynamic tidal currents, which reverse flow direction and height roughly twice a day. Tidal flows often carry a large amount of debris and sediment along the ocean bed, necessitating a design that can handle this type of abuse without requiring frequent and expensive maintenance. Current tidal turbine designs meet this set of requirements by reinforcing the blade structure, and allowing the attack angle of the blades, or orientation of the turbine itself, to be varied according to the flow direction. However, this type of design is not optimal for minimizing destructive turbulence in the wake, and poses a threat to marine life in the form of rotating blades (Lloyd-Evans, 2005). In addition, blade failure has posed a significant threat to the long-term viability of TSTs, and remains a difficult problem to tackle. The conditions under which a tidal turbine must operate are very unique, and must be negotiated while minimizing disruption to the surrounding marine ecosystem.

1.2.2 Tidal Technology

Three types of TST technologies comprise the current state of the industry, namely horizontal axis tidal turbines (HATT), vertical axis tidal turbines (VATT) and cross flow devices, as shown in Fig. 1.1. The most common types of TSTs are generally variations of the HATT, and in fact all commercial installations currently employ HATT designs exclusively. This is no doubt as a result of their similarity to wind turbines, a well understood design which, with relatively few alterations, can be adopted for use under water. The VATT is also a variation of established wind turbine technology, the main advantage of which is its ability to harness energy from flows in any direction without requiring reorientation of any kind. Cross flow devices vary dramatically in their design, but the basic principle is the same as that which guides all VATT and HATT turbine designs. Examples include helical structures, water screws and reciprocating devices, however all cross flow devices comprise only a small fraction of all tidal energy technologies.

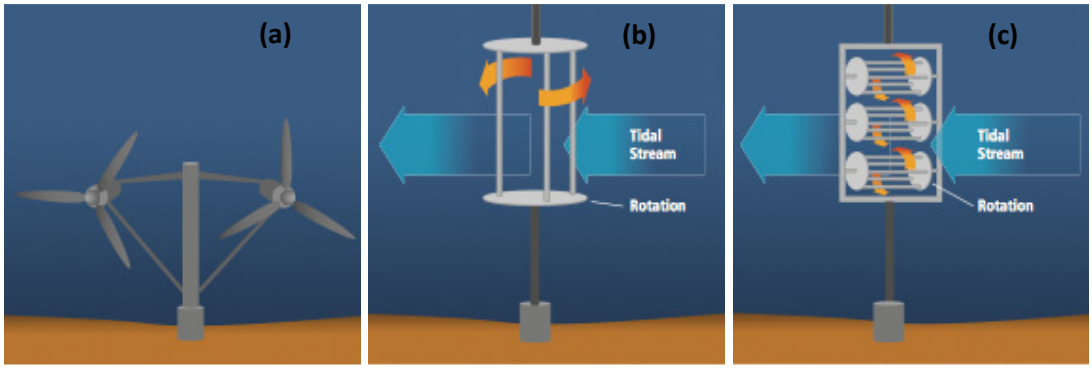

Figure 1.1. Three types of TSTs: a) horizontal axis (HATT); b) vertical axis (VATT); and c) Cross flow devices (Lewis et al., 2011)

1.2.3 The Open-Centre Turbine

Such great variety in tidal energy technology reflects both the immaturity of the industry as well as the variation in tidal stream conditions. Each marine environment is distinctly unique in terms of proximity to the shoreline, seabed character, flow depth and speed, debris content and local marine wildlife involvement. Such diversity in the conditions under which the TST must function indeed necessitates the development of many different designs each suited to a particular environment.

One design in particular, called the Open-Centre Turbine (OCT), has been developed by OpenHydro with design characteristics that make it more marine animal friendly. As is indicated by the name, this turbine features an open centre, which serves as a safe passage for

marine life, as well as debris and sediment. As shown in Fig. 1.2, the blades are fixed at both the hub and shroud, and therefore the fastest moving parts of the turbine, the blade tips, are safely housed and pose no threat to marine life. In addition, fixing the blades at both ends in this manner also provides a large increase in blade structural integrity, significantly decreasing maintenance requirements.

Figure 1.2. OpenHydro open-centre turbine (OpenHydro, 2015)

OpenHydro has developed a range of OCTs with differing power generation capabilities corresponding to a variation in the outer diameter of the turbine. The largest has an outer diameter of 20 m, and is able to produce 2 MW of electricity (OpenHydro, 2015). However all TSTs are deployed in clusters, and so the benefit of increasing the power by increasing the size of the turbine has to be weighed against the increase in the space requirements. In addition, the increase in outer diameter also limits the operation to locations that have sufficient depth so as to isolate the turbine from surface effects.

1.2.4 Proposed Design and Objective of the Present Study

The challenge of power versus size forms the impetus for this research, and has inspired the inception of an OCT design that attempts to vary power generation with turbine length instead of diameter. The Helical Open-Centre Horizontal Axis Tidal Turbine (HELIOCHATT) being investigated here also features the aforementioned advantages of the open-centre concept. However this research takes the open-centre concept even further by removing the conventional turbine blades all together and replacing the short hub and shroud with a longer tunnel on which internal veins run longitudinally and at an angle, as shown in Fig. 1.3. Rotation is imparted as the force of the current acts on the face of these veins, and due to the symmetric

nature of this structure, the turbine can operate in either flow direction without reorienting in any way. In addition, it is hoped that the channel of unrestricted flow through the centre of the turbine will contribute favourably to the wake dynamics, perhaps expediting wake dissipation and decreasing turbulence intensity. Housing the edges of the blades within the hub and shroud may present an unimpeded and safer passage to marine life, and attenuate damage to the blades from debris and sediment (OpenHydro, 2015).

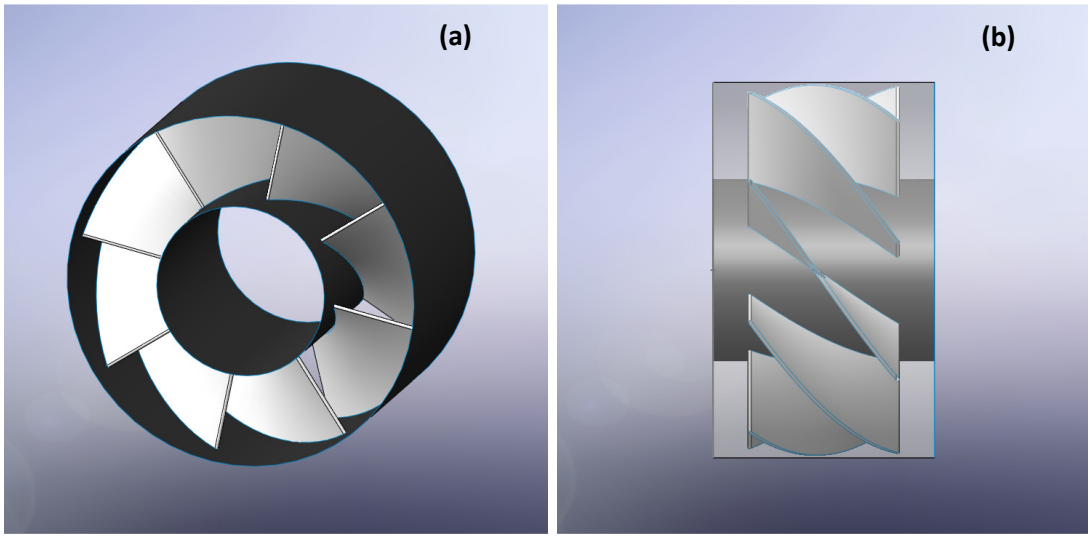

Figure 1.3. The HELIOCHATT design: (a) Isometric view; (b) Side view with transparent housing

Although the open-centre concept itself is not novel, the specific blade geometry of the HELIOCHATT is indeed a completely untested design. The focus of this research is therefore to determine the optimal blade geometry such that the turbine generates the most amount of torque while minimizing any harmful wake turbulence. The variables at play are the longitudinal length and twist angle of the blade, which together are directly responsible for the flow characteristics through the turbine. By varying the twist angle it is possible to alter the attack angle of the blade, thus changing the behaviour of the flow as it encounters the leading edge and then front and rear surfaces of the blade. Changes in the flow behaviour affect the pressure generated on the blade surfaces, thus influencing the amount of torque produced. The total surface area of the blade is directly proportional to the blade length, and so an increase in length corresponds to an increase in the surface area available to produce torque. However, the cost associated with increasing the power in this manner is an increase in the amount of drag produced by the blade as it moves through the water. Therefore it is crucial to determine at

what blade length the ratio of power to drag is greatest, and how this is affected by the twist angle.

Naturally the two parameters are concomitantly related and so a thorough study of many different design iterations is required in order to gain an understanding of the nature of this relationship. The ultimate goal of this research is to determine whether the power generation potential of the turbine can be increased through an increase in the blade length and adjustment in the twist angle. This would decrease the lateral dimension of the footprint of the structure on the seabed, making it possible to place multiple turbines closer together in a fleet arrangement. Therefore this study is designed to perform the first assessment of the HELIOCHATT design, and efficiently determine whether there exists the potential to further develop this type of turbine. The untested nature of the HELIOCHATT, featuring novel concepts including an open-centre and longitudinal blades, necessitates that this be a numerical study involving multiple design iterations. This will allow for all possible combinations of blade length and twist angle to be tested, without requiring expensive and time consuming manufacturing processes. Therefore this study involves the development of the turbine geometry, as well as the numerical model used to validate the design.

Chapter 2

2. Numerical Modelling

This chapter introduces the principles underlying the techniques of Computational Fluid Dynamics, including an explanation of the equations that govern the behaviour of fluids and some of the challenges associated with their resolution. In addition, the general process of developing a numerical representation of a turbine and the surrounding flow domain is discussed, as well as some of the most common strategies for simplifying that process. Finally, the specific numerical model used for this study is presented, and the methodology of its construction is expounded upon.

2.1 Computational Fluid Dynamics

The techniques of Computational Fluid Dynamics (CFD) have been used extensively to assess the performance of wind turbines, providing an efficient means to fully explore and develop new designs before investing in more expensive experimental trials (Sanderse et al., 2011). More recently, these same techniques have been applied to the rapidly expanding field of tidal turbine design, and now form the basis of the development and optimization process (Masters et al., 2013). Using numerical models to simulate multiple design iterations allows for the detailed analysis of power generation potential, flow behaviour around the blade structure and wake turbulence downstream for each proposed model of the turbine.

In the conceptual stages of design development there is often very little or no existing data on which to build, and so it becomes necessary to rapidly accumulate information on a very broad range of designs. A variety of methods have therefore been developed which make it possible to significantly simplify the way in which the turbine structure is represented in the simulation, thus reducing the calculation time required. The advantage of being able to quickly assess multiple design iterations using a computationally inexpensive model is most apparent when a radically new design needs to be optimized. Once an initial large scale assessment has been conducted, the list of design candidates can be winnowed down to a much smaller group of the most promising. At this point the numerical model can be significantly augmented, thus providing much more detailed information on specific design characteristics. Of course the method and degree by which the model is simplified directly impacts the accuracy of the results, and so a balance must be struck between obtaining the greatest accuracy and expending the least amount of computational resources.

2.1.1 The Actuator Disk Method

There are currently two well-established methods of turbine model simplification, and although these methods are primarily the result of decades of research into wind turbine design, they have also been successfully adapted for use in modelling tidal turbines. The most basic is called the Linear Momentum Actuator Disk Theory (LMADT), and it involves replacing the turbine rotor with a momentum sink in the form of a porous disk. In this analysis the assumption made is that velocity and pressure do not vary across the face of the turbine, and so the time-averaged effect of the rotor can be effectively smeared across a circular region. This reduces the effect of the rotor to a one-dimensional force, which acts along the rotation axis of the turbine and opposite to the direction of flow. The specific blade geometry is therefore not incorporated, and so the LMADT is a more general analysis, which determines the maximum power available to an ideal rotor.

Of course the cost of rotor simplification is a sacrifice in terms of the accuracy of the model with respect to turbulence behaviour and specific flow characteristics. Four main drawbacks to using the LMADT were identified by Harrison et al. (2010) and these limitations generally pertain to the near wake region within three to four rotor diameters (3-4D):

- There is a difference between how the model extracts momentum from the flow and how this is actually accomplished by the turbine rotor. The LMADT model simply decreases the velocity of the flow mathematically as it passes through the disk domain. However the real process is a much more complex affair in which the flow encounters the blades and loses momentum due to friction and turbulence, which in turn generates pressure differentials. The result is that the flow exiting the disk domain does not display the same turbulence characteristics, or velocity and pressure gradients across the face of the turbine as it does in the real process.
- Tip vortices are not modelled by the standard LMADT, and so any simulation requiring the analysis of such phenomenon will also require augmentation of the model to incorporate the time-averaged effect of tip vortices. This has successfully been accomplished by Sorensen and Shen (2002) through the use of the Actuator Line Method (ALM). The ALM incorporates the variation in the effect of the blades in the radial direction by revolving a line of influence, extending from the hub to shroud, around the axis of rotation. This allows for unique characteristics such as tip vortices and alternative blade geometries to be accounted for more accurately.

- The swirling behaviour of the flow as it exits the rotor section of a turbine is not captured by the non-rotating disk domain of the LMADT model. This is only relevant when studying the near wake region as the swirling generally dissipates within 4-5D. In fact, the flow dynamics within the near wake region are often excluded from scrutiny, as most wake studies are conducted only when assessing the wake interactions of multiple turbines in an array. In those cases the near wake region is inconsequential, and so the LMADT would still be a viable model.
- The LMADT is not able to report information regarding transient features of the flow such as vortices or unsteadiness in the wake. The nature of the method is such that it provides a good approximation of the time-averaged behaviour of the flow including flow velocity, pressure and isotropic turbulence. In order to capture unsteady features a large eddy simulation would need to be conducted, requiring a much greater amount of computation resources.

In summary, the LMADT provides a convenient and computationally inexpensive means by which to calculate the maximum power available to an ideal rotor. However, the significant simplification of the turbine in this manner also prevents the observation of certain flow characteristics, particularly in the wake region. This method is therefore very well suited to studies involving multiple turbine installations in which the time-averaged effect of the wake is of interest, and small-scale perturbations need not be studied.

2.1.2 The Blade Element Momentum Theory

The second method of turbine simplification is called the Blade Element Momentum Theory (BEMT), and it is in fact a combination of the blade element method and the momentum method (Lee et al., 2012). The BEMT can be used as a stand-alone model or as a component in a larger simulation. In both cases it provides information about the power generated as well as some basic description of the flow dynamics at the exit of the turbine. This technique requires the assumption that the time-averaged effect of the turbine can be represented by a circular region, and that the effect of the blades on the flow varies only with radial position. Therefore a series of radially expanding annuli can be discretized, in which the blade sections are treated as two-dimensional aerofoils. The thrust and torque forces imparted to the flow are resolved using the lift and drag coefficients corresponding to the local geometry of the blade. These forces are the source terms required by the momentum equations, which then produce information about the decrease in momentum of the flow. It is assumed that this decrease in

momentum corresponds to the amount of energy extracted by the blades and converted into torque. In summary, the annular sections can be understood as rings that absorb linear momentum and impart angular momentum to the flow (Masters et al. 2015).

Unlike the ADM model, which provides no means to account for the tangential velocity of the flow as it exits the turbine, the BEMT produces a more realistic approximation of the flow with the incorporation of aerofoil geometry. This introduces a swirl component to the exit flow, which is especially salient when the near wake region is of interest. The BEMT is also able to determine the effect of small alterations to the blade geometry on the performance of the turbine, which is useful when there is a need to account for blade tip effects and hub losses (Masters et al., 2011). The division of the rotor into discrete annuli also makes it possible to impose arbitrary inflow conditions that vary in the radial direction. In reality, the flow entering the rotor section near the distal regions of the blade has a noticeable radial component to the flow direction. This is caused by flow escaping around the outer diameter of the turbine, and can be accounted for by adjusting individual annuli boundary conditions. As with the ADM model however, the BEMT is not able to capture flow characteristics in and around the blade geometry, or accurately wake dynamics.

2.1.3 The Blade Resolved Geometry Method

In cases where all aspects of the flow through the turbine need to be studied, the aforementioned simplification methods fall short, and a fully explicit Blade Resolved Geometry (BRG) simulation is necessary. This approach involves the development of a full model of the rotor section, which is then incorporated into a rotating mesh within a fixed reference frame so as to incorporate the revolution of the blades. Using a BRG model makes it possible to study the effect of the blades on the flow, including small scale and transient effects in the flow field. The power generated by specific blade designs can be directly extracted from the simulation data without requiring assumptions to be made regarding pressure gradients, velocity profiles or lift and drag coefficients. The challenges associated with using a moving mesh are primarily related to discontinuities at the boundary between the rotating blade geometry and the surrounding flow domain, and this significantly increases the computational time (Afgan, 2013). In general, this method is only used during the study of well-established turbine designs, where an initial understanding of the behaviour of the flow has been determined. It provides very detailed information about flow behaviour, vortice formation, pressure gradients, lift and drag behaviour and power generation, however it requires an immense amount of simulation runtime.

2.2 Numerical Modelling of Fluid Dynamics

This section provides a brief description of the numerical techniques used to model fluid dynamics, however a complete overview of CFD methods can be found in standard texts such as Pope (2005) and Wilcox (1993).

The governing equations of fluid motion are derived from the fundamental laws of mechanics, and form the principles on which numerical models are built. There are three such laws, and they describe the conservation of momentum, mass and energy. The momentum conservation equation can be derived through the application of Newton's second law to the motion of fluids, and for an incompressible Newtonian fluid this yields the following (Anderson, 1995):

$$\rho \frac{\partial u_i}{\partial t} + \rho u_j \frac{\partial u_i}{\partial x_j} = -\frac{\partial p}{\partial x_i} + \mu \frac{\partial^2 u_i}{\partial x_i \partial x_j} \qquad \textbf{Eq. 2.1}$$

where ρ is the density of the fluid, p is the pressure, u_i is the i-th component of velocity and x_i is the i-th space dimension. This equation can be defined separately for each of the three dimensions, yielding the three Navier-Stokes equations. The mass conservation equation, commonly referred to as the continuity equation, is defined as follows (Anderson, 1995) for an incompressible fluid:

$$\frac{\partial u_i}{\partial x_i} = 0 \qquad \textbf{Eq. 2.2}$$

The third governing equation describes the conservation of energy, which is necessary when dealing with compressible flows and heat transfer processes. In this study it is assumed that the fluid is incompressible and any changes in temperature are negligible, therefore the energy conservation equation is not required.

The Navier-Stokes equations and the continuity equation form a set of coupled, non-linear partial differential equations, which generally cannot be solved analytically for most engineering applications of interest. Therefore various iterative methods have been developed for approximating a solution to a sufficient degree of accuracy, and are solvable using current computational techniques. These methods fall most broadly into two categories which define two fundamentally differing flow regimes, namely laminar and turbulent flow. Differentiating between these two flow regimes requires definition of the Reynolds number (Re).

This non-dimensional quantity relates the inertial and viscous forces of the flow, and is defined as follows:

$$Re = \frac{UL}{\nu} \qquad \textbf{Eq. 2.3}$$

where U is the mean flow velocity, ν is the kinematic viscosity of the fluid and L is the characteristic length of the flow. In this case the characteristic length refers to the turbine diameter. The numerator defines the inertial forces and the denominator defines the viscous forces of the flow. When the viscous forces are dominant then the fluid behaviour is laminar, and characterized by smooth flow in which the streamlines are parallel to each other and do not cross. As the inertial forces of the flow increase, and the viscosity of the fluid is no longer able to damp growing disturbances, the flow transitions to turbulent behaviour. In summary, a low Reynolds number corresponds to a laminar flow, and a high Reynolds number describes a turbulent flow.

Turbulent flow is characterized by the chaotic and unsteady motion of fluid, and contains three-dimensional vortices of differing scales. The kinetic energy of the flow is contained in large scale eddies, and is dissipated as these structures break down into smaller scale vortices. The smallest scale structures are described by the Kolmogorov micro scale, at which the kinetic energy of the large eddies is converted into the internal energy of individual molecules (Pope, 2005). The scale of the largest eddies, L is determined by the geometric boundaries of the flow, and the smallest scale, η is governed by the viscosity of the fluid. Crucially, these two length scales are related to each other by the Reynolds number as follows:

$$\frac{L}{\eta} \approx Re^{3/4} \qquad \textbf{Eq. 2.4}$$

From this it follows that as the Reynolds number increases, the difference in length scales also increases. For highly turbulent flows with very large Reynolds numbers, this creates a situation in which the temporal and spatial fluctuations vary dramatically at very small length and time scales. Therefore, resolving the flow at all length scales requires a very fine discretization scheme and a massive amount of computing power. This type of calculation is called Direct Numerical Simulation (DNS), and it is only applicable to very simple flow regimes.

An alternative to DNS is to use Reynolds Averaged Navier-Stokes (RANS) equations to solve for the mean flow characteristics. This approach requires the assumption that the

velocity variable can be decomposed into a time-averaged mean velocity component ($\overline{u_i}$) and a turbulent fluctuating component (u_i'). This type of "Reynolds decomposition" results in the following expression for velocity:

$$u_i = \overline{u_i} + u_i' \qquad \textbf{Eq. 2.5}$$

and similarly, for pressure:

$$p = \bar{p} + p' \qquad \textbf{Eq. 2.6}$$

The RANS equations are therefore the result of the decomposition of both the pressure and velocity variables in this manner:

$$\frac{\partial \mathrm{u_i}}{\partial \mathrm{x_i}} = 0 \qquad \textbf{Eq. 2.7}$$

$$\frac{\partial \bar{\mathrm{u}}_\mathrm{i}}{\partial \mathrm{t}} + \bar{\mathrm{u}}_\mathrm{j}\frac{\partial \bar{\mathrm{u}}_\mathrm{i}}{\partial \mathrm{x_j}} = -\frac{\partial \bar{\mathrm{p}}}{\partial \mathrm{x_i}} + \nu\frac{\partial^2 \bar{\mathrm{u}}_\mathrm{i}}{\partial \mathrm{x_i x_j}} - \frac{\partial \overline{\mathrm{u_\imath}'\mathrm{u_\jmath}'}}{\partial \mathrm{x_j}} \qquad \textbf{Eq. 2.8}$$

The RANS equations now contain three new variables, including a new quantity $\overline{\mathrm{u_\imath}'\mathrm{u_\jmath}'}$, called the Reynolds stress tensor. Unfortunately no new equations have been introduced, resulting in what is commonly referred to as the turbulence closure problem. Various turbulence models have been developed in order to close the system and resolve the solution, all of which involve some inherent degree of inaccuracy. The following section describes some of the most popular turbulence models.

2.3 Turbulence Modelling

Although it is not possible to solve for the fluctuating components of velocity and pressure directly, it is possible to "model", or estimate these terms by relating them to the known time averaged components. There are two general approaches to turbulence modelling, namely the Reynolds Stress Transport (RST) models and the eddy viscosity models. RST models compute all the stresses directly using the Reynolds stress transport equations, which take into account the directionality of the Reynolds stresses. This is the most sophisticated type of turbulence model, requiring a substantial amount of computation effort. The eddy viscosity

models significantly decrease the complexity of the calculation by assuming that the Reynolds stresses are isotropic, thus requiring only one or two extra equations. There are three classes of eddy viscosity models, providing different levels of accuracy. All three are based upon the Boussinesq-Approximation (Boussinesq, 1878), in which the unknown Reynolds stresses (τ_{ij}) are related to the mean velocity field via the turbulent eddy viscosity (μ_t) (Dewan, 2011):

$$\tau_{ij} = \mu_t \left(\frac{\partial \bar{u}_i}{\partial x_j} + \frac{\partial \bar{u}_j}{\partial x_i} \right) \qquad \textbf{Eq. 2.9}$$

Therefore, if the eddy viscosity can be expressed in terms of known quantities, then the game is up and the mean flow field can be determined using the aforementioned RANS equations. The following three options of eddy viscosity models propose three methods by which to achieve this lofty goal.

2.3.1 Zero-Equation Models

The zero-equation models, also called mixing length models, algebraically relate the eddy viscosity to the mean flow field variables via an empirically determined mixing length. Modifications to the model are required in order to damp the viscosity to zero as the flow reaches a solid wall. Reliance on empirical data and algebraic expressions to describe non-linear variables is clearly less than ideal, and as a result these models are considered to be incomplete (Dewan, 2011). They are appropriate for very simple flow regimes, but fall short in the presence of complex flow characteristics such as separation and cavitation.

2.3.2 One-Equation Models

These types of models offer a small increase in accuracy by including a single transport equation that can be applied to any turbulence variable, typically turbulent kinetic energy or eddy viscosity. In reality there are six transport equations, and so although using one is better than none, it is still very far from yielding a complete solution. In addition, the length scale is still provided as an input and therefore behaves as a constant, which is certainly not true for a flow displaying dynamic eddy behaviour. There is no great advantage to using a one-equation model as opposed to a zero-equation model, and as a result few exist. The most popular of the small group of contenders is the Spalart-Allmaras model (Spalart-Allmaras, 1992), which applies the transport equation to the eddy viscosity to define a new variable called the turbulent kinetic viscosity.

2.3.3 Two-Equation Models

Two-equation models introduce the first complete treatment of turbulent flow regimes by using two transport equations to model the turbulent kinetic energy as well as the turbulent length scale. Removing the need to externally define specific flow variables is an improvement over the zero and one-equation models both in terms of accuracy and convenience (Wilcox, 1993). The cost of improvement however is the addition of two extra partial differential equations, thus increasing computation time.

The equation used to model the turbulent kinetic energy is derived from the exact transport equation, and therefore there is a one to one match between the terms in the modelled equation and those in the exact transport equation. However, the equation for the dissipation of kinetic energy is derived using physical reasoning, and uses fewer terms to model its behaviour than are found in the exact transport equation. This introduces a certain amount of empiricism, and therein lies the major weakness of the two-equation models. Various attempts have been made to mitigate the adverse effects of non-exact modelling through some innovative treatments of the dissipation equation, and as a result there are now a multitude of two-equation models. All however rely on the following expressions of the turbulent kinetic energy, k and the rate of dissipation, ϵ (Dewan, 2011):

$$k = \frac{1}{2}\overline{\mathrm{u'_i u'_i}} \qquad \textbf{Eq. 2.10}$$

$$\epsilon = \nu\,\overline{\frac{\partial \mathrm{u'_i}}{\partial \mathrm{x_j}}\left(\frac{\partial \mathrm{u'_i}}{\partial \mathrm{x_j}} + \frac{\partial \mathrm{u'_j}}{\partial \mathrm{x_i}}\right)} \qquad \textbf{Eq. 2.11}$$

The following section describes some of the most relevant two-equation models, and underlines the advantages and drawbacks of each.

2.3.4 The $k - \epsilon$ Model

As is true for all eddy viscosity models, the ultimate goal is to be able to express the turbulent eddy viscosity as a function of known variables. The $k - \epsilon$ model was originally proposed by Jones and Launder (1972), and defines the turbulent eddy viscosity in terms of the

turbulent kinetic energy, k, and the kinetic dissipation rate, ϵ in the following manner (Dewan, 2011):

$$\mu_t = \rho C_\mu \frac{k^2}{\epsilon} \quad \textbf{Eq. 2.12}$$

$$C_\mu = 0.09 \quad \textbf{Eq. 2.13}$$

The $k-\epsilon$ model is derived under the assumption of a fully turbulent flow, which allows for the effect of molecular viscosity to be neglected. Modifications are required in low Reynolds number regions, such as near solid boundaries or at the laminar-to-turbulent transition layer (Wilcox, 1993). This is generally achieved by employing either wall functions or low Reynolds models. Wall functions essentially create a thin buffer zone that separates the turbulent flow from the zero slip condition at the wall, and in which the flow is not resolved using the turbulence model. Instead, the flow behaviour is described according to semi-empirical wall functions. Therefore, the boundary conditions for the turbulent flow are determined by the values calculated by the wall function at the last grid point furthest from the wall. The other method is to use low Reynolds number models, which include extra source terms in the transport equations for k and ϵ. These extra terms act as damping functions in the near wall region, and become equal to 1 further away from the wall boundary. Nevertheless, the transition from the near wall to the turbulent flow region remains an inherent weakness of all $k-\epsilon$ models.

2.3.5 The $k-\omega$ Model

The $k-\omega$ model, originally introduced by Wilcox (1993), is able to deal with low Reynolds and near wall regions without any modifications, and as such is more applicable in many situations than the $k-\epsilon$ version. This model defines the turbulent viscosity in terms of the turbulent kinetic energy, k and the specific kinetic dissipation rate, ω, which is simply a ratio of k/ϵ:

$$\mu_t = \rho \frac{k}{\omega} \quad \textbf{Eq. 2.14}$$

$$\omega = \frac{\epsilon}{k} \quad \textbf{Eq. 2.15}$$

The $k-\omega$ is reported to perform well in swirling flows and those containing highly curved streamlines, in addition to being a good near wall model. However it is also reported to be sensitive to free stream flows and free-shear flows, two conditions under which the $k-\epsilon$ is well suited. It seems then that a combination of the two models would be able to take advantage of the strengths of each, and be applicable in the greatest variety of cases. In fact such a model does exist, and it is referred to as the $k-\omega$ Shear Stress Transport (SST) model.

2.3.6 The $k-\omega$ SST Model

The $k-\omega$ SST, originally introduced by Menter (1993), incorporates a blending function in order to capitalize on the $k-\omega$'s ability to resolve boundary flows, and the $k-\epsilon$'s independence from free-stream flows. This function essentially dictates the degree to which each model contributes based on the distance from a laminar or no slip boundary. The mechanics of this calculation are presented here, where ϕ_1 and ϕ_2 represent the same turbulent variable defined by the $k-\omega$ and $k-\epsilon$ models respectively, and F_1 is the blending function:

$$\phi = F_1\phi_1 + (1-F_1)\phi_2 \qquad \textbf{Eq. 2.16}$$

In boundary layer flow the $k-\omega$ model dominates and F_1 is equal to one. However, further from the boundary layer and towards the free stream, the blending function becomes equal to zero. This then ensures that under free stream conditions the $k-\epsilon$ model dominates, with a smooth transition between the two guaranteed by the blending function.

In addition, the $k-\omega$ SST model also contains modifications to the turbulent viscosity formulation, so as to account for the transport of turbulent shear stress. This is especially important for boundary layer flows where an adverse pressure gradient leads to a greater rate of production of kinetic turbulent energy than its dissipation (Menter 1993). In conventional two-equation models this results in an over-prediction of shear stress in the boundary layer regions. In order to combat this kind of inaccuracy, the $k-\omega$ SST model uses another blending function to employ two different formulations for shear stress within the calculation for eddy viscosity (Menter 1993):

$$\nu_t = \frac{a_1 k}{max(a_1\omega; \Omega F_2)} \qquad \textbf{Eq. 2.17}$$

where a_1 is a constant and Ω is the absolute value of vorticity. In boundary layer regions the blending function, F_2 is equal to one and the shear stress is calculated from ΩF_2, and in the free stream F_2 is equal to zero and the shear stress is calculated from $a_1\omega$.

The ability to selectively employ two different models according to their areas of applicability has earned the $k-\omega$ SST model a reputation of admirable accuracy, particularly in ducted flows (Fleming et al., 2011). However, the addition of two blending functions not only increases accuracy, but also the list of functions requiring resolution, thereby increasing the computation load. For this reason, the more efficient $k-\epsilon$ model remains one of the most commonly relied upon models for turbine analysis (Masters et al., 2013), despite its lacklustre performance in the boundary layer region. In general, the $k-\omega$ SST model is resorted to only when severe separation behaviour is anticipated, or boundary layer flow is of particular interest.

2.4 Numerical Model for the Present Study

The current study aims to analyse the flow behaviour for several different turbine blade designs, some of which incorporate very aggressive attack angles and large blade surface areas. These particular blade characteristics coupled with the longitudinal nature of the design result in a very complex flow regime, displaying characteristics that change dramatically in the journey from inlet to outlet. This means that the traditional approaches to turbine model simplification presented above will not yield an accurate account of the flow behaviour or wake dynamics. Therefore a numerical approach has been developed in this study which facilitates rapid performance assessment, and which does not require inordinate amounts of computing time. The remaining part of this chapter provides an explanation of this method, including the choice of numerical turbine model, development of the mesh and strategy regarding the configuration of the CFD solver.

2.4.1 Turbine Model Development

Two conventional methods of turbine model simplification have been presented in the preceding sections of this chapter, both of which are not optimal for the current study. The LMADT method produces results that are completely independent of the specific blade design, and relies on previous data regarding pressure and velocity gradients across the turbine face. The BEM method does incorporate the effects of blade geometry, however it requires previous data regarding lift and drag coefficients as a function of radial location along the blade. The design being investigated here is the first of its kind, and therefore no data exists regarding

blade coefficients or pressure and velocity gradients. In addition, both the LMADT and the BEM methods rely heavily on the assumption of zero radial flow, a simplification that is justified for conventional rotors with a short inlet to outlet distance. However, this is simply not an appropriate assumption for the current study, where radial flow is expected to play a large role in both the power generation mechanism and wake behaviour. In summary, it is not possible to represent the turbine with a simplified model, and so a fully Blade Resolved Geometry (BRG) model will need to be developed.

As discussed earlier, a BRG model requires a much greater amount of computation time, and is indeed a much more ambitious approach. In general this kind of sophisticated simulation is only applied to turbine designs that are somewhat well established, and for which a baseline of data already exists. The aim is usually to resolve fine scale structures in the flow such as tip vortices and eddy formation, as well as to define the profile of pressure and velocity gradients along the blade surfaces. It should also be emphasised here that a BRG model is almost exclusively used in conjunction with a moving mesh, which throws another computationally expensive aspect into the mix. It would seem then that such an approach would be a ridiculous method by which to study a great multitude of designs, and likely to result in endless months of calculation.

For these reasons it was necessary to develop a type of BRG model that provides sufficient detail in the flow description but which does not require an inordinate amount of computation time. Therefore, the numerical model developed for this study incorporates two main modifications to the classical BRG approach. The first is the adoption of periodic boundary conditions along planes of symmetry, such that a single blade section can represent the entire rotor. This is a common practice in the CFD industry, and it results in a decrease in computation time proportional to the number of blades in the rotor. The illustration in Fig. 2.1 shows exactly how the rotor section can be divided, and where the planes of symmetry lie. The specific details pertaining to the periodic boundary conditions will be elaborated upon further in the following section 2.4.2.

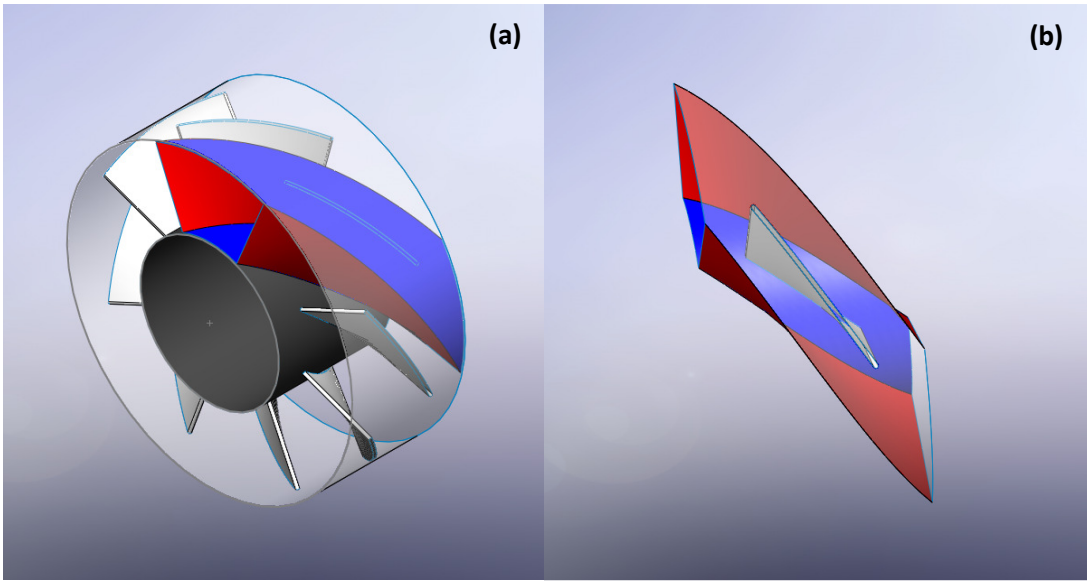

Figure 2.1. Periodic boundaries indicated in red in the (a) full turbine model; and (b) the resulting single blade flow field

The second simplification is the decision to conduct a stationary blade simulation, in which the blade is placed in a steady flow and prevented from rotating. This results in an enormous reduction in the computation time, and avoids the need for a moving mesh. Unfortunately, the accompanying compromise is a sacrifice in accuracy regarding the power generation and wake dynamics, however these conditions are applied to all the simulations equally, and so an adequate comparative analysis can still be conducted. Bearing in mind that this study is intended to identify the most promising candidates from within a pool of iterative designs, a comparative assessment is indeed the object of the present study.

2.4.2 Geometry and Mesh Development

The various blade geometries being investigated in this study have been developed using the Computer Aided Design (CAD) software SolidWorks (SolidWorks, 2014), employing a parametric design process. These 30 geometries are classified according to the blade twist angle and blade length, and a list of all permutations is presented in Appendix A. A model of the conventional open-centre turbine developed by OpenHydro has also been created, such that a comparison can be made with the new concept presented here, the HELIOCHATT design. All designs are based on an eight blade configuration, featuring a 10-m shroud diameter and a 5-m hub diameter. These are the same shroud and hub dimensions of the OpenHydro model currently in operation. Despite the obvious shortcomings of using static

blade simulations for a dynamic problem, simulating a known configuration establishes a baseline for comparison using this technique and under out current assumptions.

In order to apply the RANS equations to resolve the fluid dynamics around the blades, the flow domain must be discretized into a mesh. For this study, all the meshes are created using the commercial software ANSYS ICEM CFD (ANSYS Inc., 2009). The quality of the mesh has a large impact on the accuracy of the simulation, and the ease with which the solver is able to converge on a solution. In general, a high quality mesh should feature cells with a reasonable aspect ratio, a skewness angle greater than 18^{o}, good adherence to the geometry boundaries and a reasonable cell expansion rate. Complex geometries require very small cells in order to properly capture the fine scale features, however this requirement has to be balanced against the increase in runtime which necessarily accompanies the increase in the total number of cells in a mesh. Developing a good quality mesh is therefore a rather intricate cost-benefit type of exercise, and involves a fair amount of qualitative judgement.

Traditionally, the tendency has been to use a structured hexahedral mesh for simulations involving aerofoils in which the boundary layer behaviour is of interest. The uniform structure of hexahedral meshes makes them less taxing on solution solvers, and increases the speed of convergence. However, this type of mesh is not well suited to complex geometries, where tight curvature and sharp features are not easily modelled using square cells. Fortunately, advances in solver software capabilities have made it possible to use tetrahedral elements, which have a pyramidal shape, without hindering solution convergence or accuracy. Unstructured tetrahedral meshes are however not ideal for modelling boundary layer flow, where very strict control of the shape and expansion rate of the elements is required. In these cases several layers of prismatic elements can be grown along the surface, and then transitioned to a tetrahedral arrangement. This is exactly the method employed for this study, as shown in Fig. 2.2. The blade sections are meshed using a combination of prismatic elements along the blade surfaces, and tetrahedral elements in the remaining regions. Inlet and outlet regions are also generated and meshed using tetrahedral elements, thus creating a three-sectioned flow domain for each simulation.

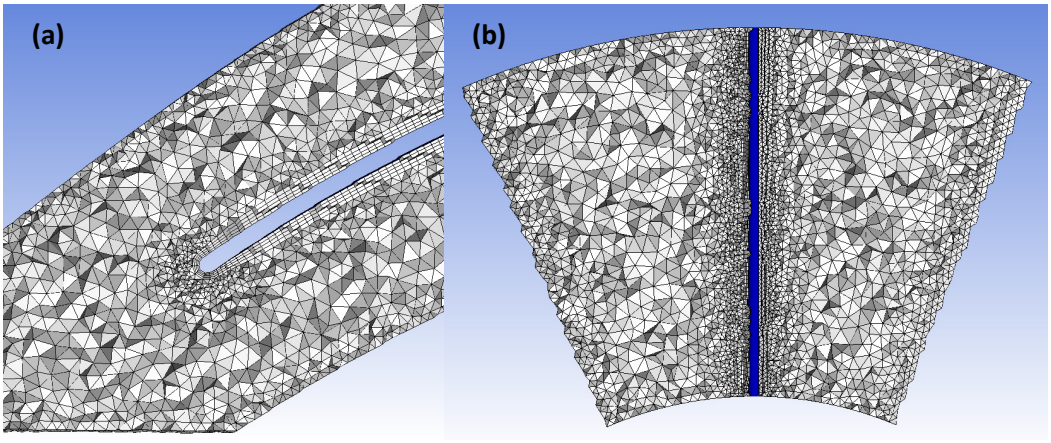

Figure 2.2. Cross section of the mesh showing (a) refinement at the leading edge of the blade, and (b) the blade section comprised of tetrahedral elements

The mesh development phase also involves the application of the periodic boundary conditions discussed in the previous section regarding the turbine model. Periodic boundary conditions are appropriate when the flow exiting through one plane is identical to the flow entering through another plane. In the case of a turbine rotor, where the flow is described as axi-symmetric, this occurs across the faces that separate blade sections. Dividing the flow domain into symmetric and repeating sectors means that the flow through the entire region of interest can be observed by resolving the flow in a single sector. However, in order to implement this kind of boundary condition CFD solvers require that the mesh topography on the periodic faces matches perfectly, and so the location of cell boundaries must be aligned.

2.4.3 Computational Fluid Dynamics Solver

The CFD solver used in this study is the commercial software ANSYS FLUENT (ANSYS Inc., 2009), which employs a cell-centred finite volume method to approximate the RANS governing equations. For this method, the flow domain has been discretized into a multitude of control volumes comprising the mesh, and so the governing equations can be integrated separately for each one. ANSYS FLUENT offers two different solution algorithms capable of performing these integrations, namely the density-based solver and the pressure-based solver. Both use a series of iterative steps to calculate the pressure and velocity fields, however the pressure-based solver is better suited to low speed, incompressible flows, and it is the one used in this study.

The coupled pressure-based solution algorithm uses a series of iterative loops to solve the pressure and momentum continuity equations simultaneously. The loop begins with an initial guess for the pressure, and then gradually updates that value using successive solutions.

Again, various methods are available within the coupled pressure-based family of solvers, all of which perform this iterative task in different ways. The one employed in this study is the PISO algorithm, which applies some additional correction factors in the process of updating the solution thereby increasing the calculation efficiency.

Of course no cell is an island, and so the calculations performed for each of these control volumes depends on the values in the surrounding cells. All variables are stored at the cell centroid, and so various spatial discretization schemes exist for calculating the values at the cell faces. This study uses the second order upwind scheme, in which the face value is determined from the values in the cell upstream. The process involves using a Taylor series expansion to extrapolate the values from the cell centre to the cell face, and then passing that value onto the neighbouring cell. In this manner the information from the surrounding cells is communicated across any cell boundaries, as it is required by the solver algorithm.

The flow regime in these simulations is turbulent, and therefore resolution of the flow behaviour requires selection of the most appropriate turbulence model, as was presented earlier in this chapter. In anticipation of a large amount of flow separation and complex boundary layer dynamics, the $k-\omega$ SST model has been chosen, and deemed most appropriate despite the increase in computation cost. ANSYS FLUENT requires the specification of two transported turbulence quantities when the $k-\omega$ SST model is applied at a boundary where flow enters the domain. For all simulations conducted during this study, the specified transported turbulence quantities chosen were the turbulence intensity and hydraulic diameter. The turbulence intensity is defined as the ratio of the root mean square of the velocity fluctuations to the mean flow velocity. Physically this can be interpreted as the degree to which the flow velocity fluctuates, or the amount of inconsistency in the velocity profile. The hydraulic diameter is used as a dimension that dictates the integral scale of the turbulence in the flow that contain energy. This helps the CFD solver to put limits on certain calculated variables, thus aiding in the convergence of the solution.

Chapter 3

3. Results and Discussion

The results presented in this chapter fall into two broad categories, the power generation potential of the new concept HELIOCHATT model, as well as a comparison of these results against those obtained for the conventional OpenHydro model. The analysis of the power generation potential is based upon measurements of the amount of torque generated about the rotation axis, as a result of the force imparted on the blade by the flow. These results are explained through a detailed study of the flow dynamics around the blade, focusing specifically on the mechanisms responsible for generating torque.

3.1 Computational Method

The numerical setup described in the previous chapter was developed as a solution to the problem of obtaining accurate results for a large number of experiments without requiring an inordinate amount of calculation resources. The method devised for this study can be classified as a fully explicit, static single blade model, which involves placing a single blade in a steady flow, and holding the blade stationary while the effect on the flow is observed. Due to the periodic boundary conditions imposed on the section faces, this essentially allows for the simulation of an entire rotor.

In reality the force of the tidal stream acting on the blade surfaces creates a rotary motion, and so by holding the geometry stationary in this study the energy that would have driven the rotation instead results in an increase in pressure on the blade surfaces. It is possible therefore to estimate the efficacy of the blade geometry, with respect to producing torque, by observing the pressure contours on the blade surfaces. Although this approach does not produce a realistic measurement of the torque produced by an equivalent physical model, it does provide a means to compare the performance of all blade geometries within the pool of design iterations. In order to gauge the relative performance of the new open-centre design being investigated here against that of the commercially produced OpenHydro turbine, a model of the conventional open-centre turbine is also assessed using the same computational method.

3.1.1 Boundary Conditions

The HELIOCHATT design features an 8-bladed rotor section, which means that each blade section spans 45^{o} of the full circumference of the rotor. In order to create a CAD model of one of these 45^{o} sections, it is necessary to slice through the hub and shroud at 22.5^{o} on

either side of the blade. The blade traces a helical curve along the hub and shroud, and so the resulting slice surfaces also follow an identical helical path, such that they remain parallel to the blade, as was shown in Fig. 2.1. This study is comprised of 30 such blade sections, each featuring a unique blade length and twist angle. Figure 3.1 shows how the variation of the length and twist angle results in a variation in the particular helix traced by the blade.

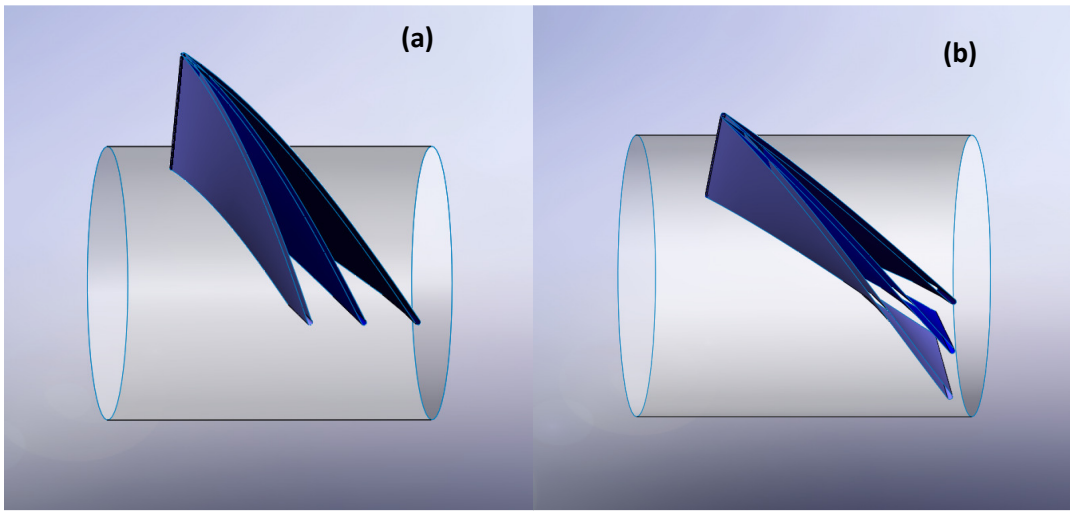

Figure 3.1. Variation in helix angle with change in (a) blade length; and (b) twist angle

All simulations conducted during this study use no-slip conditions on all solid walls, including the hub, shroud and blade surfaces. The flow is introduced at the inlet with a velocity of 2 m/s and a turbulence intensity of 5%, which are typical conditions of tidal streams in which commercial turbines usually operate (Belloni, 2013). The inlet and outlet regions are joined to the blade section via mesh interfaces, and also feature periodic boundaries on the radial slice surfaces. The curved faces of the inlet and outlet regions, which extend from the hub and shroud surfaces of the blade section, are outflow boundaries. In summary, with the exception of the velocity-inlet, all surfaces which are not solid walls or periodic faces are specified as outflow faces. The flow conditions at an outflow boundary are extrapolated from the interior flow domain, and across this surface all variables exhibit zero normal diffusive flux. This means that the pressure at any point in the flow domain is only a function of the flow conditions and not artificially controlled. This is important when considering that the performance of each blade geometry is to be determined through analysis of the magnitude of the pressure force developed on the blade surfaces. Although Fig. 3.1 shows only a selection of HELIOCHATT geometries, the same setup and boundary conditions are used for the conventional OpenHydro model.

3.1.2 Detailed Geometry Specifications

The HELIOCHATT geometries feature six different twist angles and five different blade lengths, forming a total of 30 design iterations. The twist angles range from 40° to 65° at intervals of 5°, and the blade lengths range from 2 m to 4 m at intervals of 0.5 m. For an 8-bladed rotor a twist angle of less than 45° produces 5° of uncovered rotor face per blade section, as illustrated in Fig. 3.2. Therefore by starting the twist angle range at 40°, it is possible to observe the effect of leaving part of the flow region unobstructed, as well as the effect of full coverage and blade overlap as the twist angle increases.

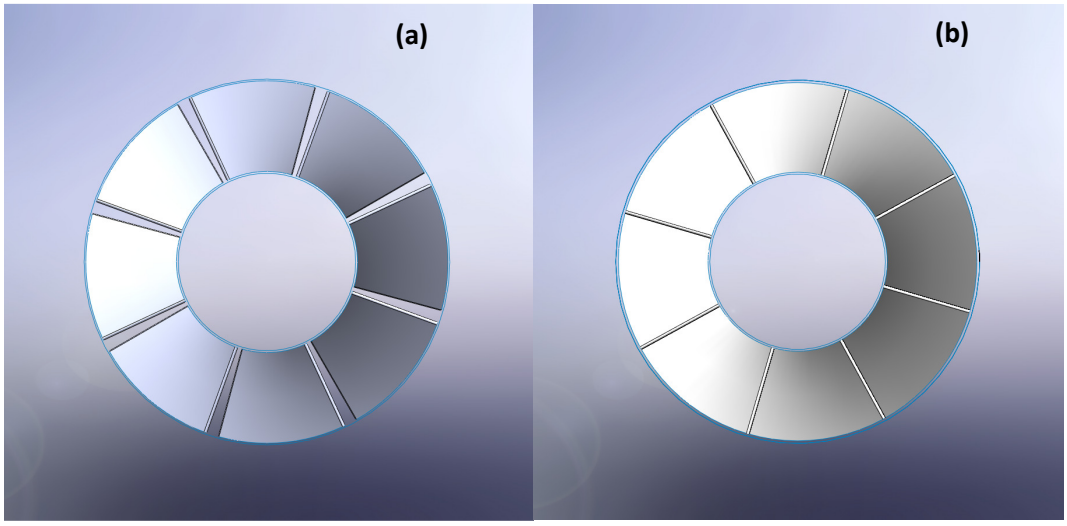

Figure 3.2. Front view of HELIOCHATT models with (a) a 40° twist angle and 5° of uncovered face; and (b) a 50° twist angle and 5° of overlap

The conventional OpenHydro turbine is based on a 12-bladed design, such that each blade section spans 30° of the full rotor face. A front view of the OpenHydro blade in Fig. 3.3 shows that the actual blade surface spans only 26° of the rotor face, leaving 4° of the flow domain unobstructed. The OpenHydro blade also features a twist angle that varies with radial location, starting at 55.5 ° at the hub and progressing to 70° at the shroud, as illustrated in Fig. 3.3. Unlike the HELIOCHATT design however, a cross section of the blade at any radial location reveals a flat surface, without a helical progression. These dimensions are based on the research by Carlson et al. (2014), which was sponsored by the U.S. Department of Energy.

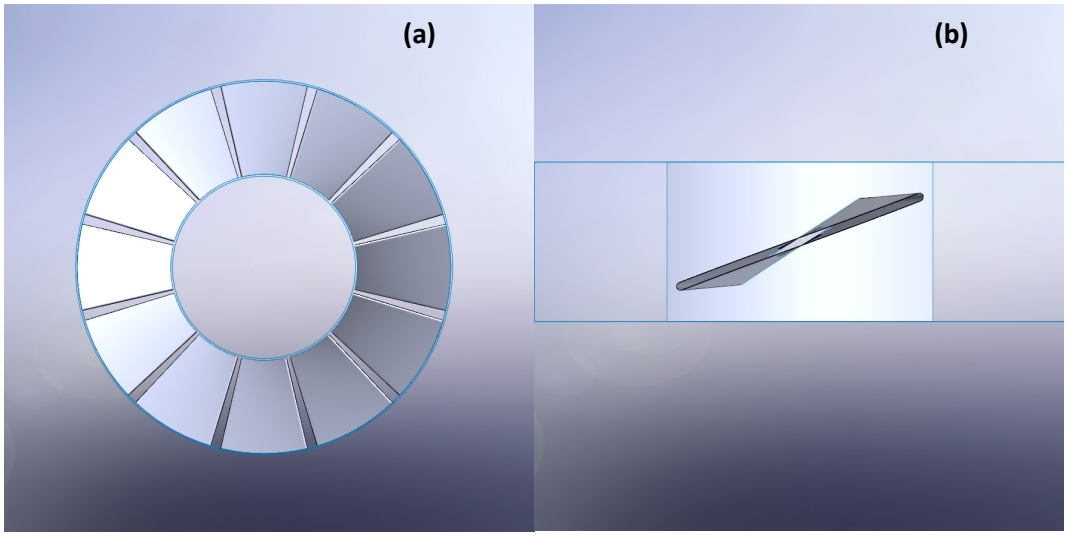

Figure 3.3. Front view of the OpenHydro model showing (a) a blade span of 26° leaving 4° uncovered; and (b) the top view showing a variable twist angle

In an effort to isolate the effects of blade twist angle and length from any other contributing factors, the HELIOCHATT designs all feature the same hub and shroud dimensions as the OpenHydro model. The hub therefore has a diameter of 5 m, which produces an unobstructed passage through the centre of the turbine measuring 19.6 m^2. The shroud measures 10 m in diameter, such that the entire rotor face spans a 78.5 m^2 surface area, of which 58.9 m^2 encompasses the bladed section.

It should be noted that the HELIOCHATT design is based on an 8-bladed rotor, as opposed to the 12-bladed design of the OpenHydro model. The reason for decreasing the number of blades is to facilitate the analysis of large twist angles, without overcrowding the rotor and introducing an unreasonable amount of interference in the flow behaviour between blade sections. As the twist angle increases the perpendicular distance between the blade faces narrows, thus forcing the flow travelling along the rear surface of one blade to interact with the front surface of its neighbouring blade. This type of interaction is indeed an inherent feature of the flow field surrounding all turbine rotors, and therefore it would be impossible and in fact undesirable to eliminate completely. However in the present study it is necessary to maintain at least a certain level of blade independence, such that the unique features of the flow field around the helical blade are identifiable. Therefore in order to make an honest comparison between the OpenHydro and HELIOCHATT models, despite using a different number of blades, all designs were analysed based on the performance of a full rotor. This means that the values obtained from a single OpenHydro blade are multiplied by 12, and the HELIOCHATT values are multiplied by 8. A non-dimensional analysis is then carried out on both sets of data.

3.2 Power Generation Potential

A tidal turbine generates electricity by using the kinetic energy of the tidal stream to rotate the blades of the turbine, which in turn drive a generator housed in the stationary component of the structure. Although a great variety of turbine designs have been created for this purpose, they all generally rely on a pressure differential of some kind to drive the rotation of the blades. The method of power generation can therefore be distilled to a relatively simple concept; in order to create a moment about the rotation axis a high pressure must be developed on one side of the blade while a low pressure is developed on the opposite side. Therefore, in the turbine design process a large emphasise is placed on determining the ideal blade geometry such that the maximum amount of power can be extracted from the tidal stream. However, just as there can be no absolute consensus on the perfect wing design for an aircraft, there is also no single best turbine design. Instead, for each broad design category, including VATTs and HATTs, a range of blade designs should be examined and the performance benefits of each should be determined. This study is focused on obtaining a better understanding of the benefits of an open-centre type of design, with respect to its ability to generate the maximum amount of torque.

3.2.1 Torque Generation

Torque is generated when a force is exerted at some distance from an axis of rotation, and in the most general case it is calculated as follows:

$$M_T = F \cdot d \qquad \textbf{Eq. 3.1}$$

where F is the force exerted, and d is the perpendicular distance from the axis of rotation. In the case of a turbine blade, the force is imparted by the flow encountering the blade surface, which occurs along the entire length and on all surfaces of the blade. As mentioned earlier, the force is in fact generated as a result of the pressure of the flow acting on the blade surface, and is calculated as follows:

$$F_p = P_T \cdot A \qquad \textbf{Eq. 3.2}$$

where P_T is the local total pressure on the blade, and A is the area on which it acts. Total pressure is the combination of static and dynamic pressure, and is therefore a function of the

flow velocity. This means that the magnitude of the total pressure is not constant across the blade surface, and so the magnitude of the force generated by the total pressure also varies with location on the surface. Therefore, in order to calculate the total amount of torque generated by the blade, an integration of torque must be performed across each blade surface. For this study, the blade surfaces have all been divided into small areas comprising the surface mesh, and so the integration is performed by summing together the torque generated by each cell. The following section describes the method by which local cell values are determined, and used to calculate the amount of torque produced by each blade geometry.

3.2.2 Calculation of Torque

Forces generated by pressure always act perpendicularly to the surface, and in this case the two surfaces of interest are the front and rear faces of the helical blade. Both blade faces are comprised of a multitude of triangular cell faces, each of which forms one end of a prismatic cell. The magnitude of the pressure force acting on each triangular cell area, can be calculated using a slightly modified version of Equation (3.2):

$$F_{p_c} = P_T \cdot A_c \qquad \textbf{Eq. 3.3}$$

where F_{p_c} is the magnitude of the perpendicular pressure force acting on the cell, and A_c is the magnitude of the triangular cell area.

Although this pressure force acts perpendicularly to the cell face on the blade surface, the cell face itself is not perpendicular to the axis of rotation of the turbine. Instead, the nature of a helical blade is such that it traverses the length of the turbine with a constant angle, referred to as the helix angle. Therefore the pressure force must be assessed as a vector quantity, and decomposed into those components that contribute to torque production and those that do not. Decomposition of the pressure force vector requires determination of the helix angle, which is calculated as follows:

$$\varphi = \tan^{-1}\left(\frac{2\pi r}{l_p}\right) \qquad \textbf{Eq. 3.4}$$

where φ is the helix angle, r is the radius of the hub, and l_P is the pitch of the helix.

The pitch is simply the axial distance traversed by the helix if it was to make one full revolution of the hub, and is calculated as follows:

$$l_P = \frac{360°}{\alpha} \cdot l_b \qquad \textbf{Eq. 3.5}$$

where l_b and α are the length and twist angle of the blade respectively. Once the helix angle has been determined, the pressure force vector can be decomposed into its axial and tangential components, as it is only the tangential component which contributes to the generation of torque:

$$\overrightarrow{F_{p_t}} = \overrightarrow{F_{p_c}} \cdot \cos\varphi \qquad \textbf{Eq. 3.6}$$

The torque produced by each cell can then be calculated by multiplying the magnitude of the tangential pressure force by the cell's radial distance from the rotation axis:

$$M_{T_c} = F_{p_t} \cdot l_r \qquad \textbf{Eq. 3.7}$$

The total amount of torque produced by the entire blade is then the summation of the torque produced by all the cell faces on both the front and rear blade surfaces.

The same procedure is followed in order to calculate the torque produced by the conventional OpenHydro model, however obtaining the twist angle requires a slightly different approach. The OpenHydro blade does not follow a helical path, but instead features a twist angle that varies with radial location from 55.5 ^{o} at the hub to 70^{o} at the shroud. Therefore in order to obtain the tangential pressure force acting on any cell face, the local twist angle must be determined and used to decompose the perpendicular pressure force. The twist angle varies linearly from hub to shroud, and so is a function of the radial location:

$$\alpha = 55.5° + \left(5.8° \cdot (l_r - 2.5)\right) \qquad \textbf{Eq. 3.8}$$

The twist angle must therefore be calculated independently for each cell on both blade surfaces of the OpenHydro model before the total amount of torque can be determined using Equations (3.6) and (3.7).

As mentioned earlier, each HELIOCHATT blade design is analysed based on the performance of a full rotor of 8 blades, and compared to the performance of a 12-bladed OpenHydro rotor. This is achieved by assuming that a full rotor of HELIOCHATT blades will produce 8 times as much torque as a single blade, and that the interaction between blades will be taken into account through the use of periodic boundary conditions. Similarly for the OpenHydro model, the performance of a single blade is multiplied by 12. The final analysis is performed in a non-dimensional manner by calculating the coefficient of torque for a full rotor of each blade design, according to the following formula:

$$C_T = \frac{M_{T_r}}{\frac{1}{2}\rho V^2 AR} \qquad \textbf{Eq. 3.9}$$

where M_{T_r} is the total torque produced by a full rotor, V is the free stream velocity of the flow, A is the swept area and R is the radius of the rotor. The coefficient of torque, C_T is essentially a measure of how well the blade converts the momentum of the flow into torque, and is therefore a means to gauge power generation potential.

3.2.3 Grid Resolution Study

In order to eliminate sources of error in the results related to grid resolution sensitivity, a number of different mesh resolutions were tested and compared. This makes it possible to balance computation time with solution convergence and accuracy. Four different mesh resolutions are presented here, however these represent only the most pertinent examples from a larger group of candidates. The results of the study are presented in Fig. 3.4, which demonstrates the relationship between the number of mesh elements and the amount of total torque produced by the blade. The mesh study shows that a decrease in mesh resolution leads to a progressive decrease in reported total torque. However, when compared to the results of the mesh with the greatest resolution, the maximum deviation is less than 1%, reported by the mesh with the worst resolution. Therefore the grid resolution chosen for this study matches that of the mesh with the third finest discretization, which limits the element size to a maximum of $5\text{x}10^{-4}\ \text{m}^3$.

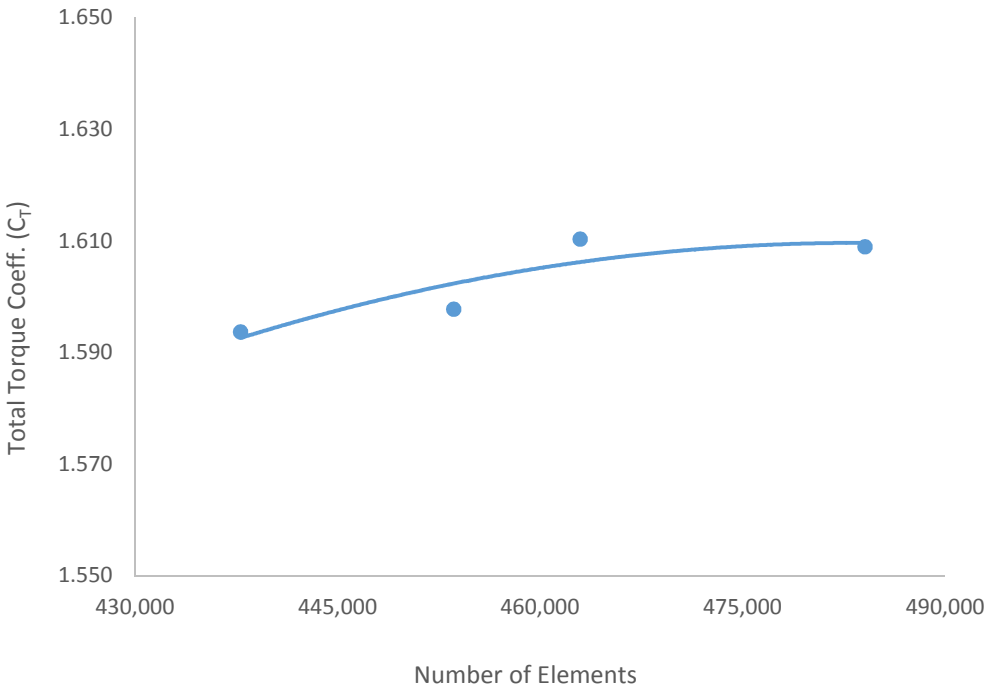

Figure 3.4. Total torque produced by 2-m 40^o blade for different mesh sizes

Number of Elements	% Difference
438,000	0.95
453,000	0.69
463,000	0.09

Table 3.1. Maximum deviation in reported torque with decreasing grid resolution

A qualitative assessment of mesh resolution is also conducted through the use of pressure contour plots, the details of which will be elaborated upon in the following sections of this chapter, but which essentially provide a visual description of the pressure profile around the blade. The pressure contours presented in Fig. 3.5 show the same cross-section view of the flow domain corresponding to the three different mesh sizes. The almost identical nature of these contour plots supports the assertion that the results of the simulations are sufficiently independent of the grid resolution.

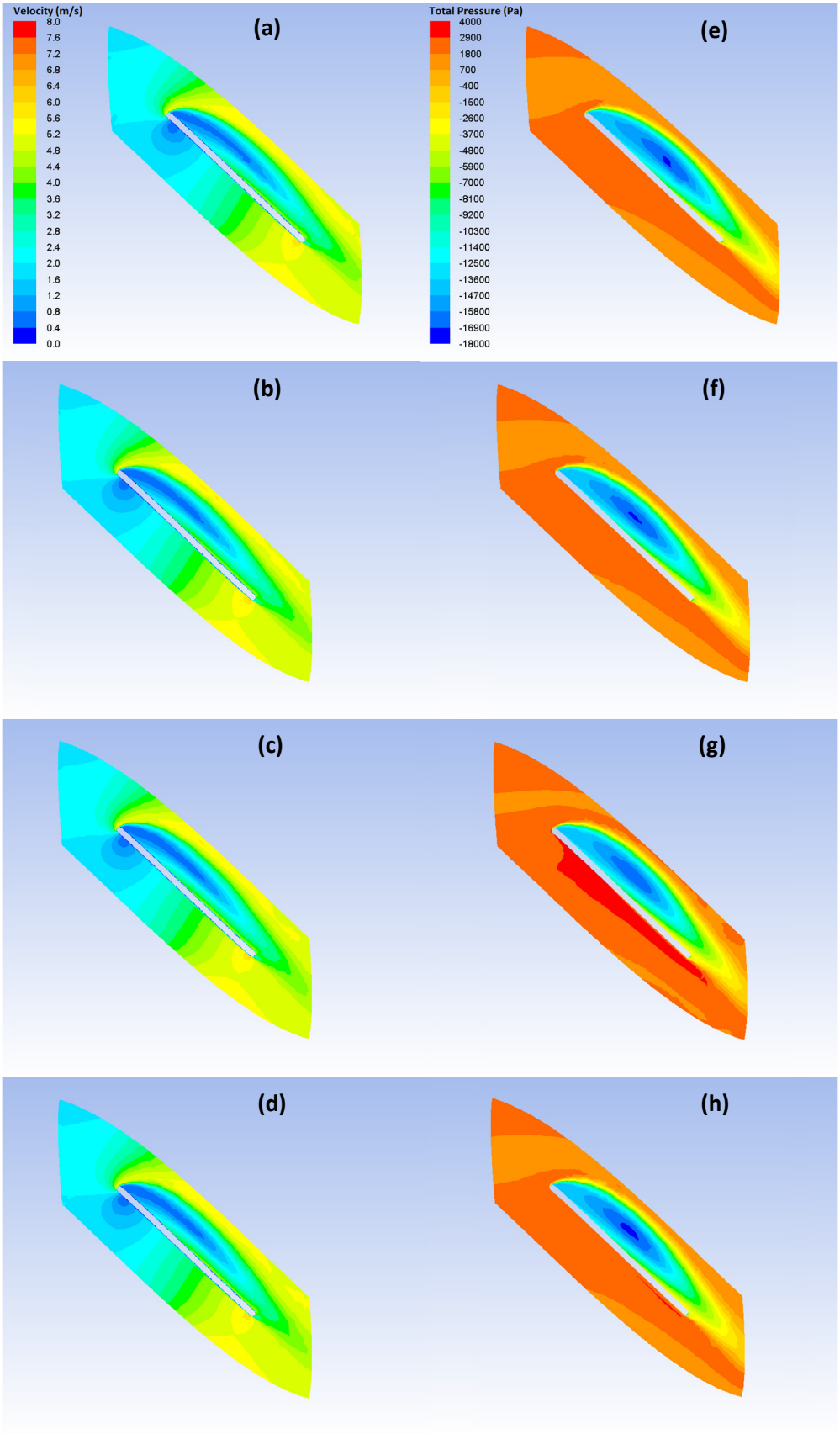

Figure 3.5. Contour plots of 2-m, 40^{o} blade showing velocity in (a) to (d); and total pressure in (e) to (h) for meshes of decreasing size

A total of 30 different geometries were tested, resulting in as many different meshes, however each one was developed using the same standard mesh resolution. This results in a difference in the total number of elements per mesh; the range of mesh size is tabulated in Table 3.1

Twist Angle	Mesh Range
40°	455,000 – 593,000
45°	459,000 – 605,000
50°	469,000 – 630,000
55°	485,000 – 665,000
60°	580,000 – 627,000
65°	583,000 – 643,000

Table 3.2. Table of mesh sizes per class

3.3 Results of Torque Calculations

The graphs presented in the following section show the results of the torque coefficient calculations, and are presented in several ways so as to highlight important relationships between performance and blade geometry. The term *class* will be used to specify all blades of the same twist angle, and the term *platoon* will refer to those with the same blade length.

Fig. 3.6a presents a comparison of all the blade geometries by plotting the total torque coefficient for each case, and grouping the results into their respective twist angle classes. Fig. 3.6b presents the same data, but groups the results into blade length platoons. From these first graphs it is clear that the power generation potential is very much a function of both twist angle and blade length. In fact two trends in behaviour are immediately obvious; an increase in twist angle corresponds to an increase in torque, while an increase in blade length results in a decrease in torque. It is also important to note that the 2 m and 2.5 m blades are more sensitive to an increase in twist angle, whereas the 3 to 4 m blades are less so. The initial design recommendation then is that in order to increase the amount of torque generated, it is most useful to increase the twist angle rather than the blade length. This conclusion will be expounded upon in the following part of this chapter.

3.3.1 Static and Dynamic Torque

As mentioned previously, the torque coefficients presented in Fig. 3.6 are calculated using the total pressure, which is a combination of static and dynamic pressure. However, in order to understand the trends in torque performance, it is useful to consider the individual contributions of the static and dynamic pressures separately. Therefore the torque coefficients are also calculated using the same method presented earlier in Section 3.2.2, but using the values for static and dynamic pressure. The results presented in Fig. 3.6c show that while both contribute positively to the torque generation, it is the static pressure which has a more significant impact, and which dominates in setting the general trend in torque behaviour. Figure 3.6c also shows that the torque generated by the static pressure, referred to here as the "static torque", decreases with an increase in blade length, while the opposite is true for "dynamic torque" which increases. A brief discussion about static and dynamic pressure is now required in order to correlate these trends in static, dynamic and total torque.

The static pressure can be understood as the thermodynamic pressure of the fluid, or the pressure felt by a particle moving with the flow. Consider such a particle, referred to here as the Test Particle (TP), which moves with the same velocity as the flow, but which is "static" with respect to other particles around it. If the flow is unobstructed and all the particles are free to move in the same general direction, then the TP will experience a constant pressure due to the random movement and consequent impact of neighbouring particles. This random movement of particles is more formally referred to as internal energy, and it is responsible for generating the static pressure of the flow, which is measured in Pascal.

Now consider the effect of placing an obstruction in the flow, and how this influences the TP's experience. If the TP is one of the particles which impacts and stagnates on the offending surface, then it will experience a dramatic increase in the rate and magnitude of collisions with other particles arriving from upstream. In effect, the TP will experience a transformation of the kinetic energy of upstream particles into a percussive force as they suddenly encounter a stationary TP. This percussive force is more commonly referred to as the stagnation pressure. The difference between the pressure felt by the TP while moving with the flow and while stagnated on the surface is defined as the dynamic pressure. Note that before

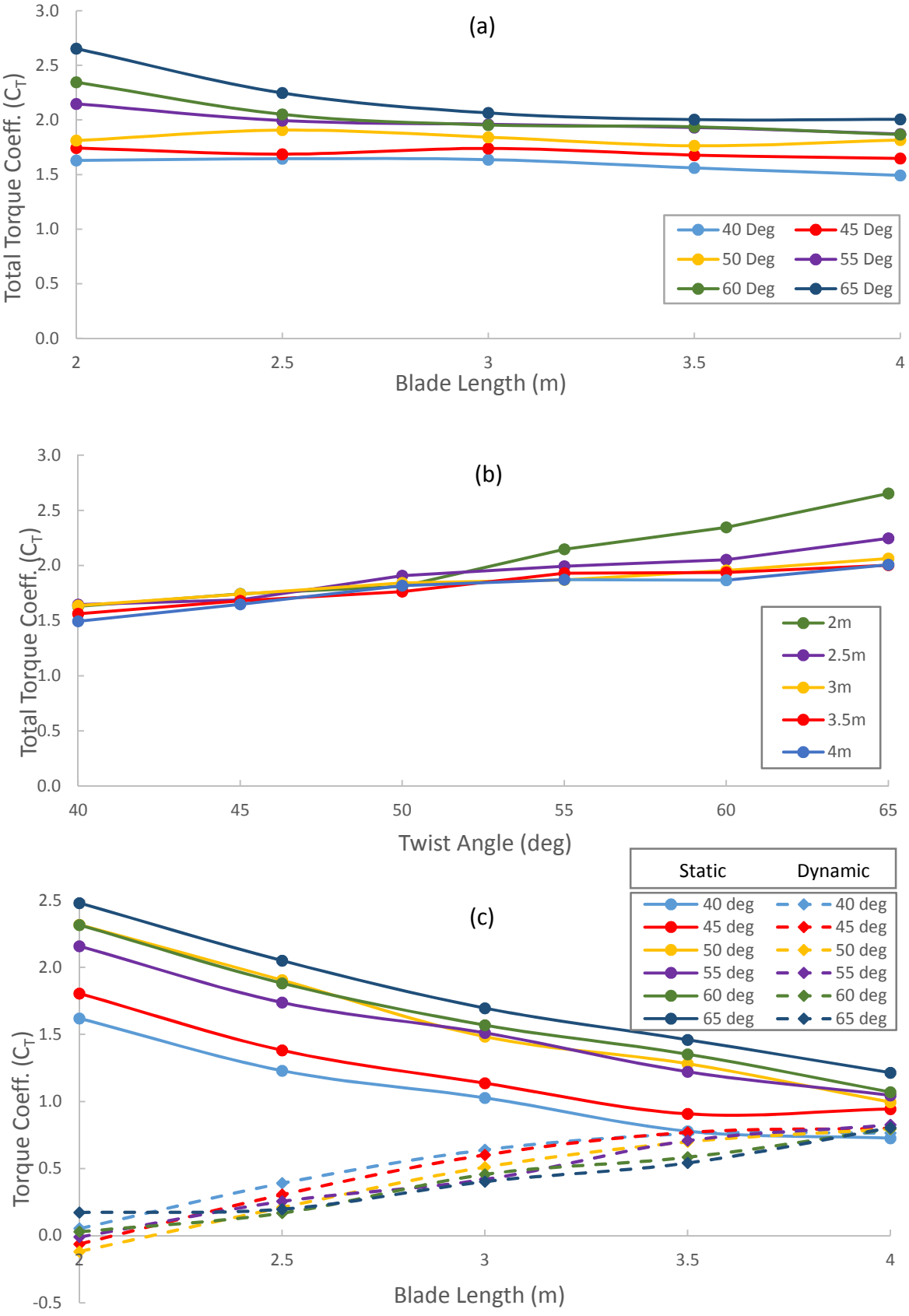

Figure 3.6. Coefficient of (a) total torque, C_T, for each twist angle class (b) total torque, C_T, for each blade length (c) static, C_{Ts}, and dynamic torque, C_{Td}, for each twist angle

the upstream particles encounter the TP, the dynamic “pressure” of the flow is not actually experienced as a pressure, but is instead more accurately described as a measure of the kinetic energy of the flow. Despite the fact that the physical meaning of dynamic pressure differs quite significantly from the classical definition of pressure as a force over an area, it is also measured in Pascal.

3.3.2 Influence of Blade Length over Performance

At this point it is still unclear why the data presented in Fig. 3.6 shows that the static torque decreases with blade length and the dynamic torque increases. This requires establishing the individual contributions to the overall production of torque of the front and rear surfaces of the blade. The best illustration of front and rear surface torque performance is through the use of pressure and velocity contour plots, which provide a qualitative means by which to examine the data. Contour plots are essentially two-dimensional slices of the flow domain on which the magnitude of a given variable may be mapped. In this case it is most instructive to extract these plots at a constant radial distance from the axis of rotation, specifically half way between the hub and shroud. The first set of contour plots shown in Fig. 3.7 are maps of the velocity magnitude and dynamic pressure for each blade length within the 40^{o} class. Each image is oriented such that flow enters the turbine from the left and exits through the outlet on the right hand side.

The most noticeable phenomenon is an area of low velocity located along what will be referred to as the rear surface of the blade. This is caused by flow separation from the blade surface, and the formation of a recirculation zone. Although every blade length within the class features a low velocity zone, the location, size and shape vary. At blade lengths of 2 m and 2.5 m the recirculation zone is completely detached from the blade surface and extends only part way from the leading to trailing edge of the blade. For blade lengths of 3 to 4 m the recirculation zone reattaches to the rear surface, and then extends all the way from the leading to trailing edge, see Fig 3.7. This is explained by the difference in attack angle of the blade, which is directly related to the blade length.

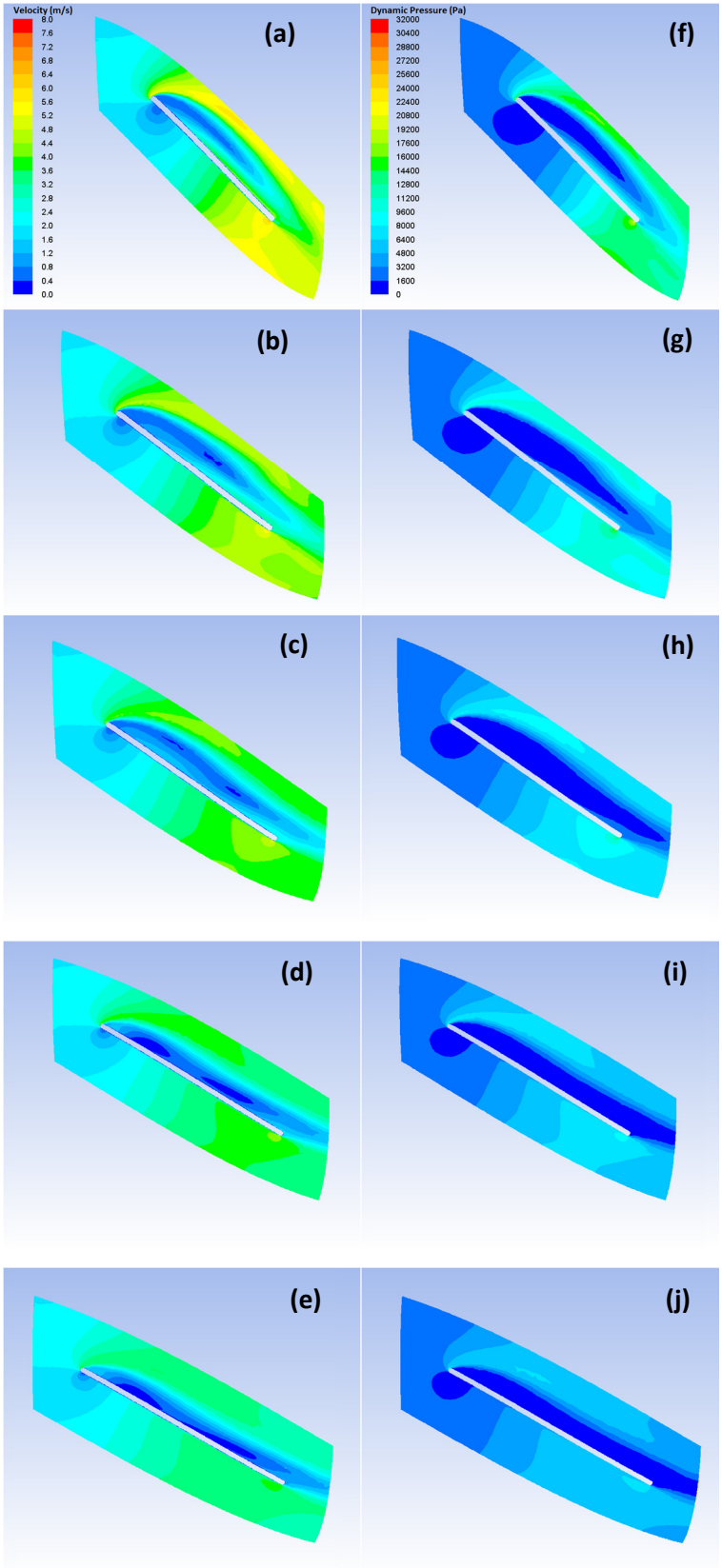

Figure 3.7. Contour plots of 40^{o} class showing velocity profiles in (a) to (e) and dynamic pressure profiles in (f) to (j) corresponding to an increase in blade length of 2 to 4 m

Similarly to an aircraft wing, the angle the blade makes with the incoming flow is referred to as the attack angle. If the twist angle is held constant, the attack angle decreases as the blade length is increased. The more aggressive the attack angle, the more difficult it is for the incoming flow to follow the rear surface of the blade, as this requires a dramatic change in momentum. In all cases, the flow encounters the leading edge of the blade and makes an effort to travel parallel to the rear surface, however it fails to do so if the rear surface is at too great an angle. Instead, the momentum of the flow carries it away from the rear surface and into the recirculation zone. This creates an absence of flow in the region between the recirculation zone and the rear surface of the blade. This in turn drives some of the flow from the tail end of the recirculation back along the rear surface, but in the opposite direction, from trailing to leading edge, as shown in the velocity vector plot in Fig. 3.8. This counter flow, as it shall be referred to, has a greater velocity than the flow trapped in the recirculation zone so it is at a higher dynamic pressure. It follows then that when the recirculation zone is detached, as occurs at the two shortest blade lengths, the dynamic pressure along the rear surface increases due to the presence of the high speed counter flow. However, when the low velocity recirculation zone reattaches, as occurs at the longer blade lengths, then the dynamic pressure decreases along the rear surface.

The development of this kind of turbulent recirculation zone behind the blade is somewhat analogous to the flow dynamics which occur along the low pressure surface of an aerofoil in deep stall. In general, as the attack angle of an aerofoil is increased the amount of lift it produces also increases. However, if the attack angle becomes greater than what is referred to as the critical angle, the amount of lift produced drops off sharply and drag increases significantly. This results from the presence of flow separation along the low pressure surface of the aerofoil, and the development of a turbulent region which resembles that of the recirculation region seen in each of the contours presented in Fig. 3.7. Therefore it is interesting to note that flow separation is undesirable when attempting to produce lift using an aerofoil, but seems to play an important and positive role in the torque performance of the HELIOCHATT blade geometries. This is undoubtedly at least in part due to the periodic nature of a turbine rotor, and the effect that each blade has on the flow dynamics around its neighbour.

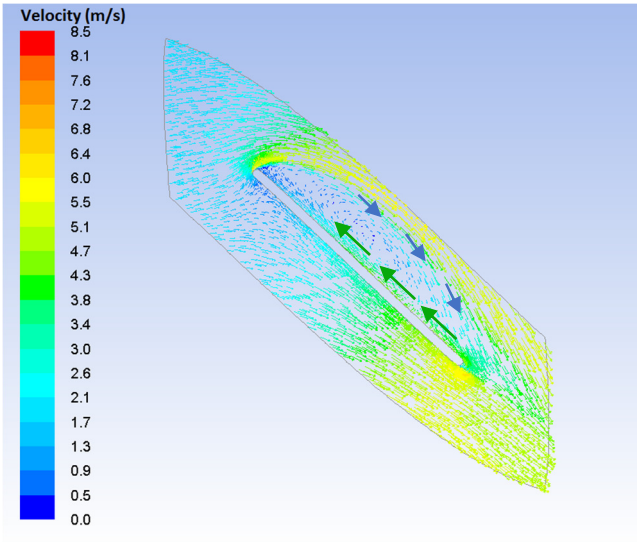

Figure 3.8. Velocity vector plot showing counter flow

The flow dynamics of the front side of the blade are slightly less exotic, featuring neither recirculation nor counter flow. In all cases, as the flow encounters the front surface of the blade, a localized stagnation region forms near the leading edge. The shorter the blade length the more pronounced this stagnation region becomes, and this is due to the more aggressive attack angle of the blade. In this stagnation region the flow impacts the blade surface and is either redirected back towards the leading edge and around the back side of the blade, or along the front side. The majority of the flow does the latter, and is easily able to follow a path which runs parallel to the blade surface. Without having to negotiate the dynamics of recirculation and counter flow, the front surface flow is able to maintain a higher velocity, and therefore a higher dynamic pressure than the rear surface. In fact the dynamic pressure along the front surface of the blade remains relatively constant, even as the blade length increases.

The differing trends between front and rear surface dynamic pressure behaviour are illustrated in Fig. 3.9, in which the dynamic torque produced by each surface are plotted as a function of the blade length. As it is a pressure differential which drives the torque production of the blade, it is the difference between the front and rear surface pressures which is of interest. This plot shows that the difference in dynamic torque experienced by the front and rear surfaces increases as the blade length increases, and this is in large part due to the drop in pressure along the rear surface. The relatively constant dynamic pressure along the front surface, paired with the initial high dynamic pressure along the rear surface that gradually decreases, explains the increase in the dynamic pressure differential with the increase in blade length. This increasing

pressure differential causes an increase in the dynamic torque, a trend which is reflected in Fig. 3.6c presented previously.

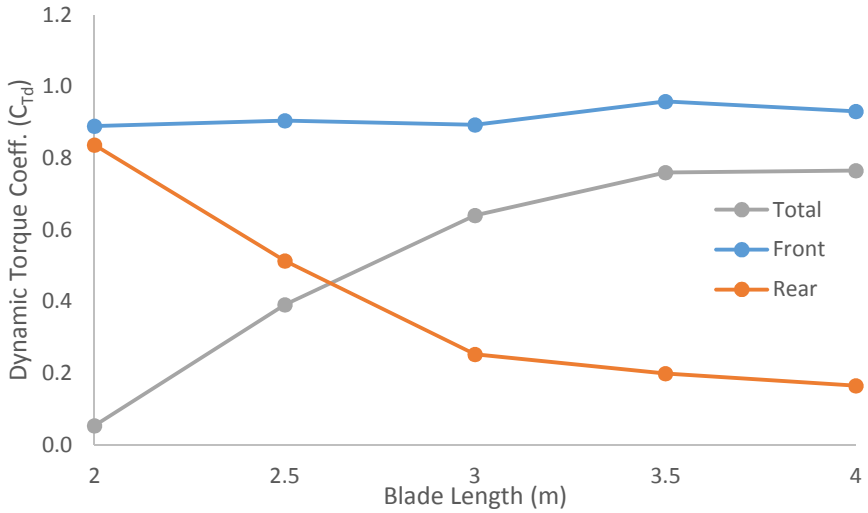

Figure 3.9. Dynamic torque coefficient, C_{Td} of front and rear surfaces of 40° blade

A different trend in behaviour is observed when the static torque is plotted as a function of the blade length. For any given twist angle, Fig. 3.6c shows that as the blade length is increased, the static torque decreases. This behaviour is also best illustrated using contour plots. However, in this case the magnitude of both the static pressure and the total pressure are mapped. The images presented in Fig. 3.10 show these contours for the 40° class, extracted at the same radial location as those shown in Fig. 3.7. As was the case for the dynamic torque behaviour, the trend in static torque is also driven predominantly by the flow dynamics occurring near the rear surface of the blade.

As is shown in Fig. 3.10, the aggressive attack angle of the 2-m blade creates an area of low static pressure behind the blade, again due to flow separation from the rear surface. As the blade length increases and the attack angle decreases, this low static pressure region shrinks, and eventually becomes almost unidentifiable. The static pressure is related to the level of boisterous interaction between water molecules; the greater the velocity at which the molecules collide, and the rate at which they do so, the greater the static pressure. Therefore in regions where the mean kinetic energy is high, the static pressure is also high. Conversely a low mean kinetic energy usually corresponds to a low static pressure, and this is the case in the recirculation region. The reason for this decrease in kinetic energy is indeed the phenomenon which lies at the heart of turbulence modelling. The process begins with an injection of energy

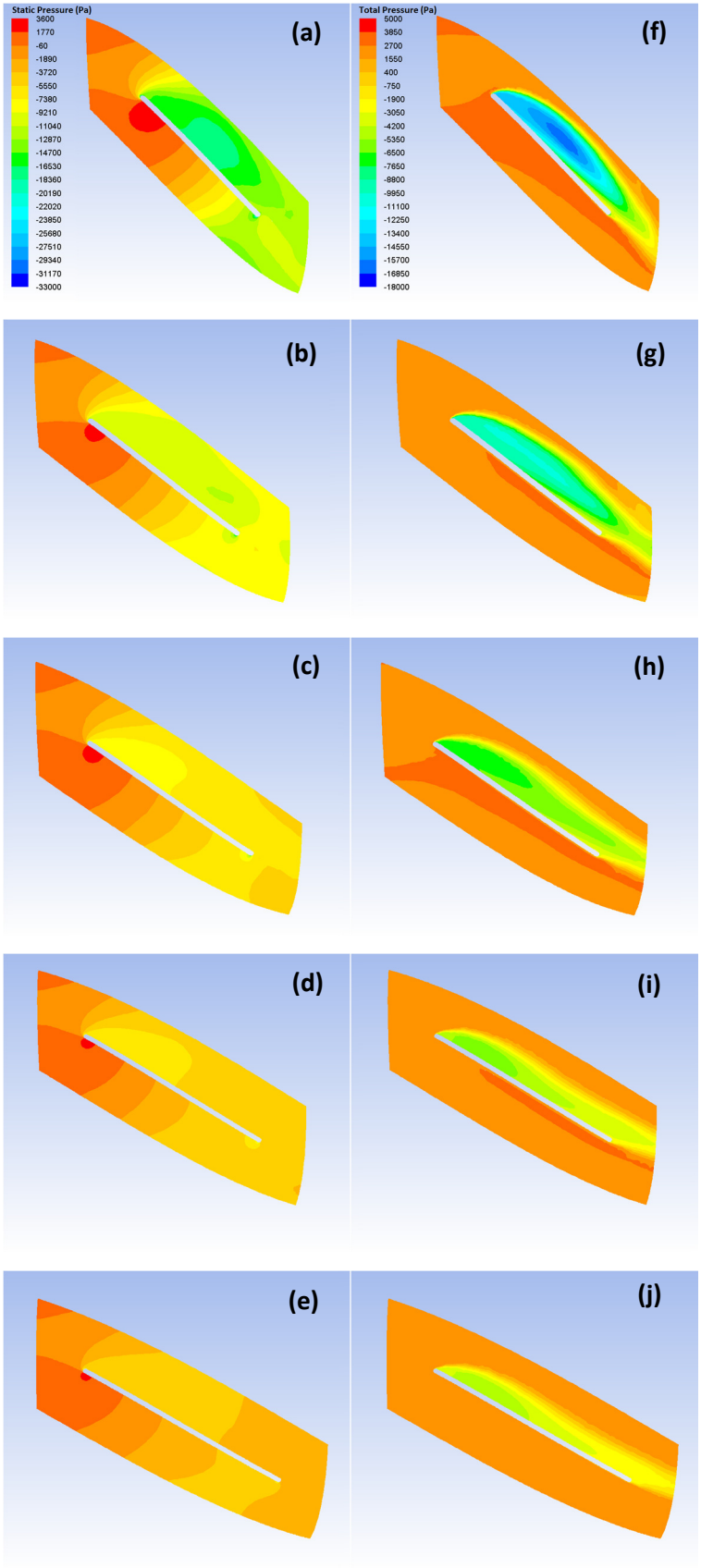

Figure 3.10. Contour plots of 40^{o} class showing static pressure profiles in (a) to (e) and total pressure profiles in (f) to (j) corresponding to an increase in blade length of 2 to 4 m.

into the flow from some driving force; in this case the flow is simply introduced with a specific velocity and kinetic energy at the inlet of the blade section. A certain amount of the mean kinetic energy of the flow is then converted into turbulent kinetic energy through inertial effects. The turbulence finally dissipates that energy into heat through viscous effects at a rate which is referred to as the turbulent kinetic dissipation rate. In summary, turbulence is essentially a complicated mechanism by which the mean kinetic energy is sapped and converted into heat. This is very clearly illustrated in Fig. 3.11 by the contour plots on the left which present the turbulent kinetic energy, and the velocity vector plots on the right. The vectors have been coloured according to the turbulent kinetic energy, and their length indicates the velocity magnitude.

Although the static pressure contours in Fig.3.10 do indeed demonstrate how the turbulence can affect the static pressure in the method mentioned above, the correlation is not precisely matched. This is due to the fact that static pressure is also influenced by other characteristics of the flow, such as flow stagnation. Clearly the stagnation point on the front surface near the leading edge is a region of low velocity, however the static pressure here is in fact much greater than in the low velocity recirculation region. This is due to the method by which the flow velocity is decreased, and the effect which is recorded by a change in internal energy. As the flow is brought to an abrupt halt on the surface of the blade, a significant amount of kinetic energy is suddenly concentrated on a small area of the blade. The flow arriving from upstream experiences an abrupt change in momentum, as a large part of its kinetic energy is transformed into internal energy, thus increasing the static pressure. Therefore it is the combination of turbulence as well as other internal flow characteristics which gives rise to the final profile of the total pressure, which is shown in Fig 3.10.

The static pressure on the front side of the blade is greater than on the rear side for all blade lengths, however the difference in magnitude between the front and rear static pressures is greatest at the smallest blade lengths. This is primarily due to the low pressure region in the recirculation zone, which shrinks in size and magnitude as the blade length increases. The amount of static torque generated by the blade is a function of the static pressure differential across the front and rear surfaces, and in this respect the shorter the blade length the more

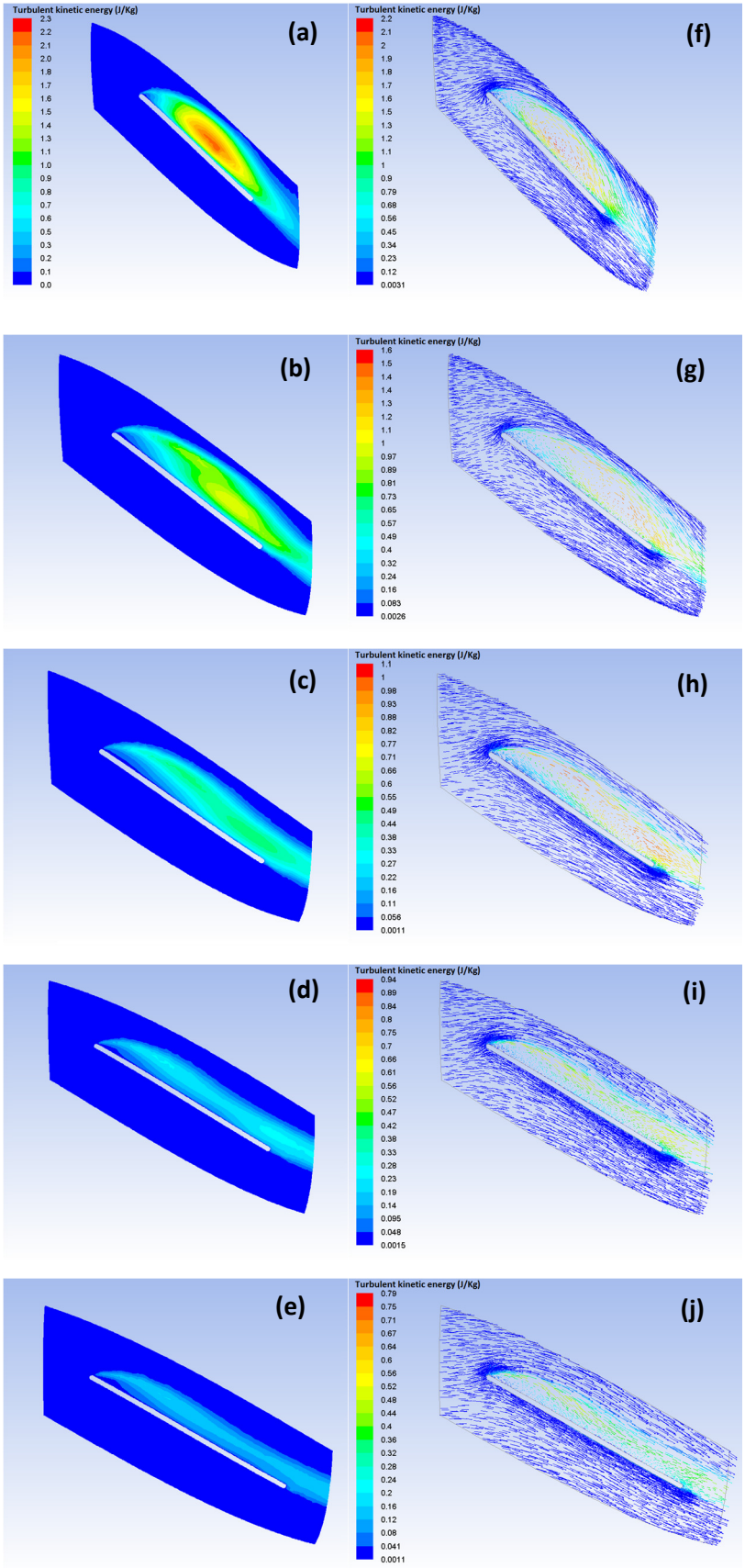

Figure 3.11. Contour plots of 40^{o} class showing turbulent kinetic energy profiles in (a) to (e) and velocity vectors coloured to show turbulence in (f) to (j) corresponding to an increase in blade length of 2 to 4 m

effective it is at generating a static pressure differential. This is best illustrated in Fig. 3.12, in which the individual contributions of the front and rear surfaces to the total amount of static torque produced is evaluated at each blade length.

The total amount of torque produced by the blade is a function of both the static and dynamic torque. Therefore the combination of the downward trend of the static torque with the upward trend of the dynamic torque, with respect to an increase in blade length, produces the final total torque trend presented in Fig. 3.6a. In all cases the contribution of the static torque is more significant than that of the dynamic torque, and it is the general downward trend of the static torque which is reflected in the total torque production trend.

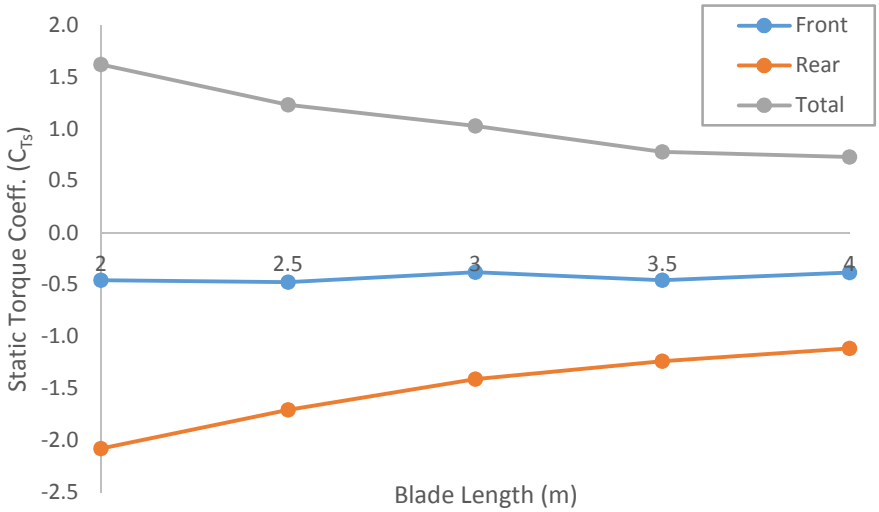

Figure 3.12. Static torque coefficient, C_{Ts} from front and rear surfaces of 40° blade

3.3.3 Influence of Twist Angle over Performance

The contour plots presented thus far all pertain to the 40° class, and so the following section presents a similar assessment of the blades within the 65° class for comparison. The general trend in performance as a function of blade length is in fact very similar across all twist angle classes, however the magnitude of the total torque produced by the different classes does vary. It will become clear that this is in fact due to the change in attack angle as well as the distance between neighbouring blades, both of which are a function of blade length and twist angle.

In dealing with the 40° class it was shown that for a given twist angle, the attack angle decreases with an increase in blade length. It should then be noted that the converse is true for an increase in twist angle; for any given blade length, an increase in twist angle results in an

increase in attack angle. This is due to the fact that the blade must traverse a greater circumferential distance around the hub in order to cover the larger twist angle. Another important effect of increasing the twist angle on blade geometry is the narrowing of the passage between neighbouring blades, through which the flow is forced to travel at increasing velocity. Although the number of blades remains constant, the perpendicular distance between the front side of one blade and the rear surface of the next decreases as the twist angle increases, as shown in Fig. 3.13. The blades then act as a nozzle, forcing the incompressible flow to speed up as it enters the blade section. The increase in attack angle and decrease in the distance between blades are both results of an increase in twist angle, and have a great impact on the performance of the blade.

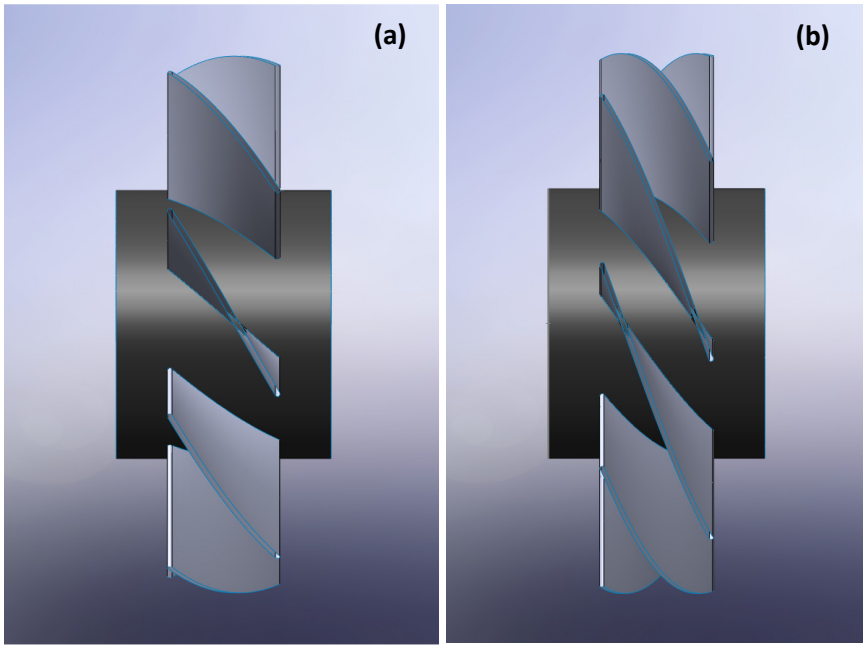

Figure 3.13. Narrowing of passageway

The dynamic torque performance of the 65^{o} class is again investigated using contour plots of the velocity and dynamic pressure, which are also taken at a radial distance that is half way between the hub and shroud, as shown in Fig. 3.14. The same low velocity zone develops near the rear surface of the blade as a result of flow separation and recirculation, which are themselves both products of the aggressive attack angle. A significant amount of high speed counter flow is produced along the rear surface as a result, causing an increase in dynamic pressure along the entire rear surface.

The presence of the low velocity recirculation zone also has the effect of further narrowing the already tight passageway between neighbouring blades, thus forcing the flow to

accelerate. The flow is now squeezed between the recirculation zone on the rear surface of one blade and the front surface of another. This would have the effect of increasing the velocity of the flow on the entire front side of each blade, if it were not for the stagnation zone which develops on the front surface near the leading edge. The presence of the stagnation zone prevents the high speed flow from contacting a large part of the front side of blade, and so a high velocity region can only be observed on the downstream section of the front surface. Fortunately, the velocity of the high speed flow is sufficiently great, and it gains access to enough surface area, that it is still able to create a relatively high dynamic pressure on the front side of the blade. Unfortunately the high speed counter flow is able to do the same on the rear surface of the blade, and so the dynamic pressure differential across the blade suffers, resulting in a poor dynamic torque performance. In summary, the short blade lengths are not able to generate a large amount of dynamic torque because both the front and rear surfaces of the blade are exposed to a high velocity flow.

An increase in blade length affects the two low velocity zones differently; the less aggressive attack angle of a longer blade produces a smaller stagnation region on the front surface and a larger recirculation region on the back surface. The stagnation region on the front side shrinks slightly as the front surface of the blade makes less of an angle with the incoming flow, and therefore presents a smaller effective surface area. However the influence on the stagnation region is actually rather minimal, and therefore does not greatly impact the performance of the front surface. The easing of the attack angle does however have a noticeable influence over the size and location of the recirculation region, which becomes more elongated along the rear surface. This results from a broadening of the passageway between neighbouring blades, and a decrease in the velocity of the high speed flow passing through that gap.

For short blade lengths and narrow passageways, the high speed flow is not only squeezed into a narrow corridor, but it also is forced to come in contact with the downstream portion of the rear surface of the blade. This ricochet action causes the high speed flow to impinge on the tail end of the recirculation zone, preventing the low velocity zone from extending further towards the trailing edge of the blade. As the passageway broadens and the ricochet lessens, the recirculation zone grows in the downstream direction. The final result is

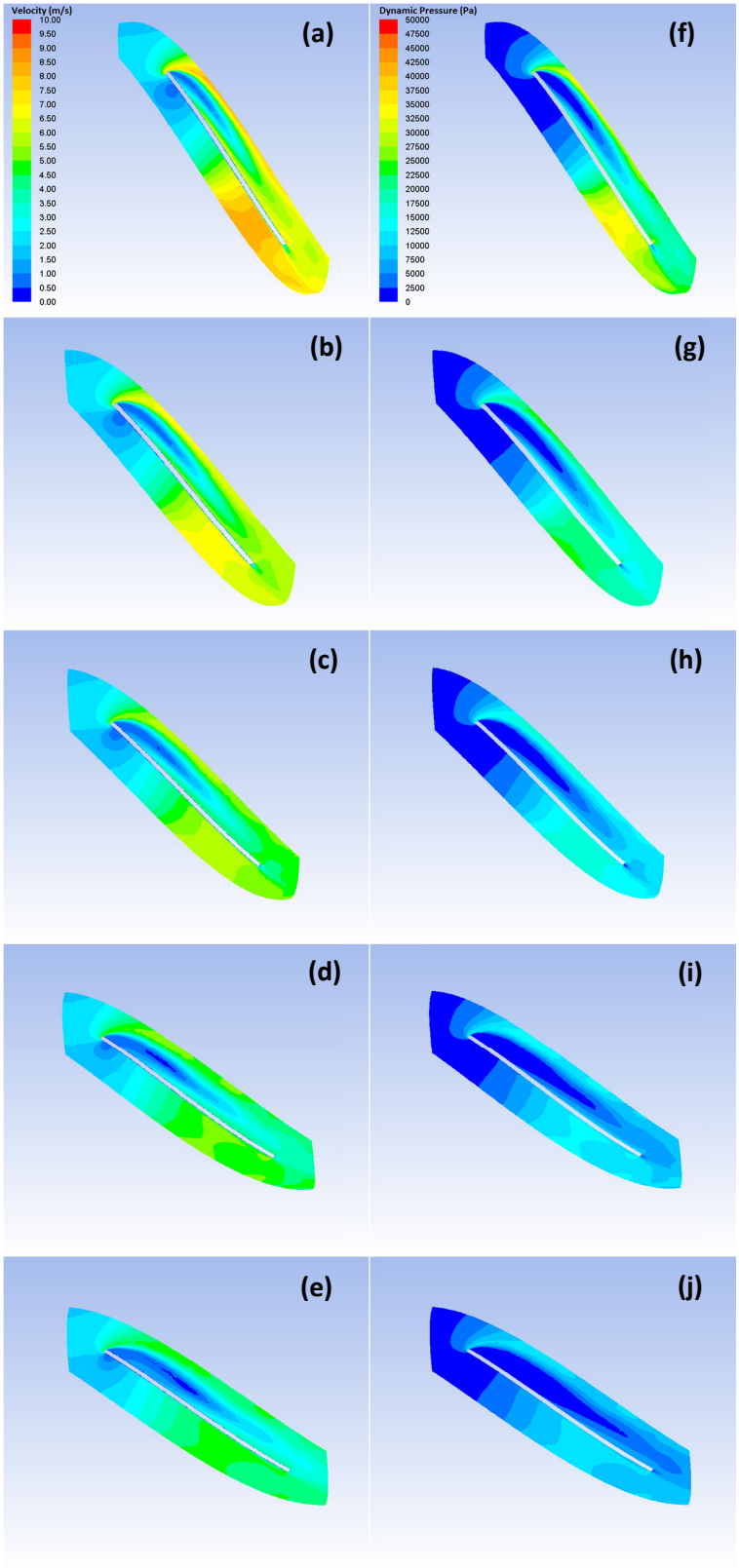

Figure 3.14. Contour plots of 65° class showing velocity profiles in (a) to (e) and dynamic pressure profiles in (f) to (j) corresponding to an increase in blade length of 2 to 4 m

the exposure of a larger portion of the rear surface of the blade to the low velocity flow of the recirculation zone. Therefore the increase in blade length causes the rear surface to produce less dynamic torque, which is the same effect observed in the 40° class, although for slightly different reasons. The overall effect of blade length on the total amount of dynamic torque produced, as well as the individual front and rear contributions, is presented in Fig. 3.15. It has been established that the static torque performance is of more importance than the dynamic torque, as it the static pressure differential across the blade which is responsible for producing the majority of the total torque. Therefore to illustrate the static and total torque performance of the 65° class, the contour plots in Fig. 3.16 present the static and total pressure profiles.

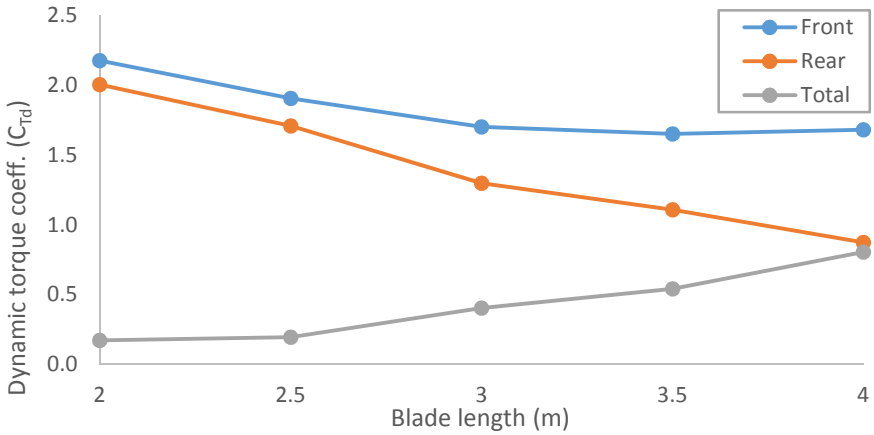

Figure 3.15. Dynamic torque coefficient, C_{Ts} from front and rear surfaces of 65° blade

These plots show that the shorter blade lengths are again more capable of producing larger static pressure differentials, and this is directly as a result of the recirculation zone behind the blade and the stagnation region on the front surface. The reasons for the development of the low velocity recirculation region have been sufficiently elaborated upon during the discussion regarding the dynamic torque performance, suffice to say that it is a function of the attack angle of the blade. The static pressure within the recirculation zone drops significantly as a result of the turbulent behaviour of the flow, and in fact this drop in static pressure is almost twice as dramatic as was seen in the 40° class. The magnitude of the drop in static pressure is a function of the magnitude of the turbulence within the rotational flow, as well as the size of the region itself. The profile of the turbulence region with respect to magnitude and effective area is a function of the attack angle, with an aggressive angle producing a smaller but more turbulent recirculation region. This more concentrated region of turbulence is in fact more

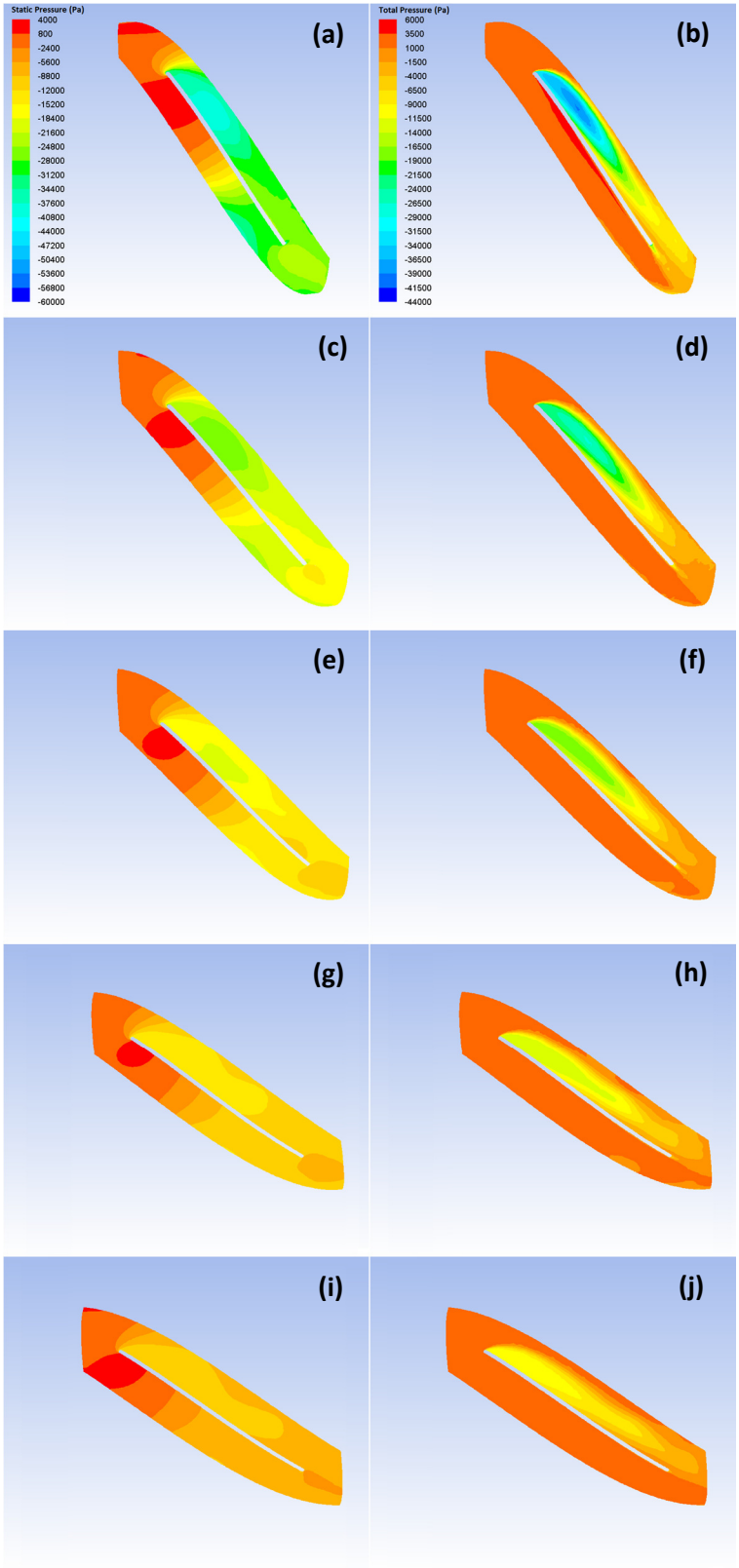

Figure 3.16. Contour plots of 65^{o} class showing static pressure profiles in (a) to (e) and total pressure profiles in (f) to (j) corresponding to an increase in blade length of 2 to 4 m

effective at decreasing the static pressure behind the blade, accomplished through turbulent dissipation. Essentially, the shortest blade with the largest twist angle features the most aggressive attack angle, and therefore produces the most pronounced turbulent recirculation region with the lowest static pressure.

In addition to the low static pressure generated by the recirculation region, which occurs along the upstream portion of the rear surface, is the low static pressure generated by the high speed flow along the downstream portion of the rear surface. Although this occurs at all blade lengths, it is most pronounced in the shortest blades. The narrow passageway caused by a short blade length and large twist angle is again responsible for directing the high speed flow onto the downstream portion of the rear blade surface. The high velocity of this flow stream creates a low static pressure, and so extends the low static pressure region from the tail end of the recirculation region all the way to the trailing edge of the blade. As the blade length increases, and the ricochet action of the high speed flow lessens, the static pressure along the rear surface increases. In summary, the aggressive attack angle produces a low static pressure on the upstream portion of the rear surface due to the recirculation region, and on the downstream surface due to the ricochet of the high speed flow. Consequently the shorter blade lengths feature the lowest static pressure along the entire rear surface of the blade.

For all blades within the 65^{o} class, the low static pressure on the rear surface is paired with a high static pressure on the front surface, generated primarily as a result of the stagnation region near the leading edge. The largest stagnation region occurs in the shortest blade lengths which feature the most aggressive attack angles, and so the shorter blades would be expected to generate the most amount of front surface static torque. However, the high speed flow generated by the narrow passageway also impacts the downstream portion of the front surface of the blade, thus creating a low static pressure on part of that surface. As the blade length increases, the size and magnitude of the stagnation region decreases only slightly, but the effect of the high speed flow decreases more significantly. The overall effect of a longer blade length is a front surface which generates more static torque.

The assessment thus far shows that the average static pressure on both the front and rear surfaces of the blade increases with blade length. Therefore in order for the length to influence the amount of static torque produced by the blade as a whole, there must be a difference between the rate at which the static pressure increases on the front and rear surfaces. It is the rear surface which in fact shows a greater increase in static pressure as the blade length increases, and so the general trend in static torque performance of the entire blade is downwards. This is due to the fact that both the upstream and downstream portions of the rear

surface experience an increase in static pressure as both the recirculation and high speed flow phenomena dissipate. Conversely, the front surface experiences an increase in static pressure only on the downstream portion of the blade which is exposed to the high speed flow. This behaviour is illustrated in Fig. 3.17, which presents individual front and rear static torque contributions.

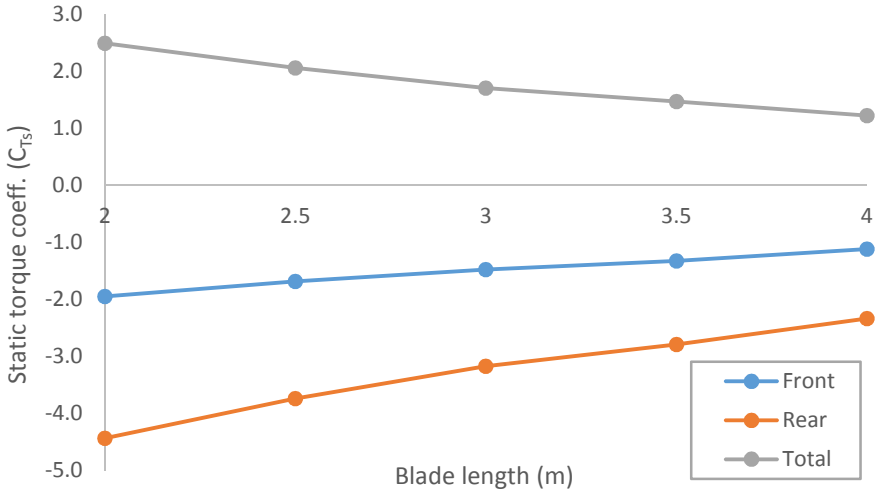

Figure 3.17. Static torque coefficient, C_{Ts} from front and rear surfaces of 65° blade

The flow behaviour around the blade is certainly a complicated situation, composed of several smaller phenomenon which are all entwined in a symbiotic relationship. In order to tie together these somewhat independently explained mechanisms, it is the turbulence contours which prove most useful. Examining the turbulent behaviour of the flow provides the clearest link between the dynamic, static and total pressure profiles, and so contour plots of the turbulent kinetic energy are presented here in Fig. 3.18. Note first that the dynamic pressure is basically a measure of the mean kinetic energy of the flow, and therefore the dynamic pressure plots from Fig 3.14 are in fact maps of that kinetic energy. Also bearing in mind that turbulence dissipates kinetic energy, it follows then that the turbulent kinetic energy contours and the dynamic pressure contours match quite well. The effect of turbulence is also evident in the static pressure profile, where the turbulent recirculation region is indeed also a region of low static pressure. However, the static pressure of the flow is influenced by more than just

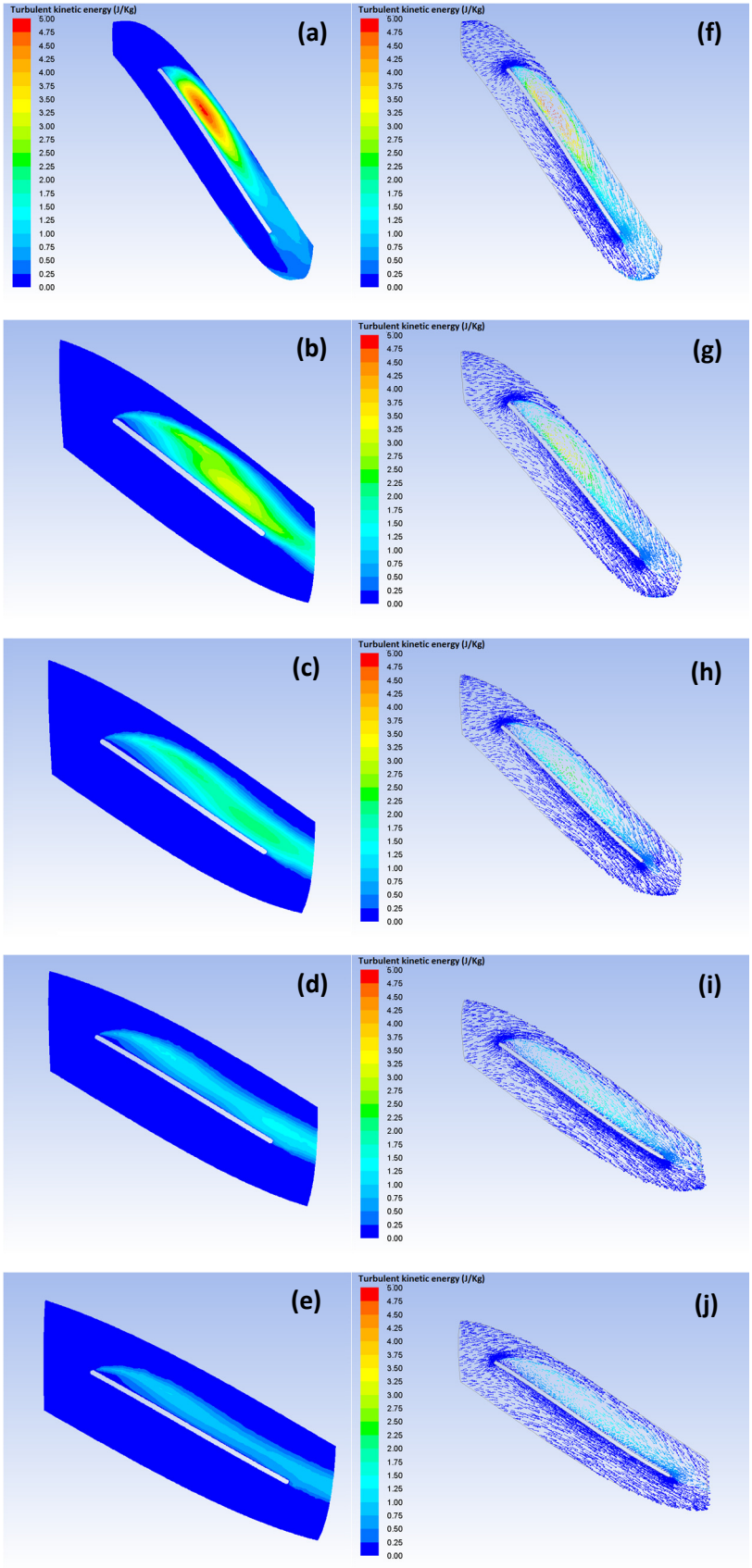

Figure 3.18. Contour plots of 65^{o} class showing turbulent kinetic energy profiles in (a) to (e) and velocity vectors coloured to show turbulence in (f) to (j) corresponding to an increase in blade length of 2 to 4 m

turbulence, and in this case that is illustrated by the stagnation region on the front side of the blade. Here the conversion of kinetic energy into internal energy produces a high static pressure where the flow stagnates, which occurs despite the absence of turbulence. Finally, the static and dynamic pressure profiles can now be combined to produce the total pressure profiles from Fig. 3.16.

The final assessment of the performance of the 65° class is that the shortest blade lengths produce the most amount of static torque and the least amount of dynamic torque. As the blade length increases, the static torque decreases and the dynamic torque increases, producing two competing trends in performance. The amount of static torque produced at any blade length is much greater than the amount of dynamic torque produced, so the general trend in total torque follows that of the static torque. This is the same result reached in the examination of the 40° class, which also showed that the shortest blade length was the most effective torque producer. Furthermore, the 65° class produces more torque than the 40° class at each respective blade length, leading to the conclusion that a larger twist angle is advantageous. Combining these two findings results in a statement about the performance of every blade tested during this study; the most effective design is the shortest blade with the largest twist angle.

3.3.4 Performance of Conventional Openhydro Model

A model of the conventional open-centre turbine developed by OpenHydro was also tested using the same numerical setup, so an analysis of the torque generation potential of the OpenHydro model is presented in this section. The total amount of torque produced by the blade is calculated based on the total pressure differential, as was the case for the preceding HELIOCHATT design assessment. Indeed an evaluation of the total torque shows that The OpenHydro model was outperformed by all but three blades within the 55 to 65° HELIOCHATT classes, as shown in Fig. 3.19. This graph presents the total torque coefficients for each blade length within the 55°, 60° and 65° classes, and in each case compares the performance of the HELIOCHATT blades with that of the OpenHydro model. It should be noted that the OpenHydro model is only 1.5 m in length, and the shortest HELIOCHATT blades measure 2 m. The variation in blade length is one of the fundamental changes implemented in the inception of the HELIOCHATT, so it is precisely a comparison between the shorter non-helical OpenHydro blade and the longer helical version featured in the HELIOCHATT which is needed. With this in mind, the performance of the OpenHydro blade is compared to all blade lengths from the HELIOCHATT range in the following discussion.

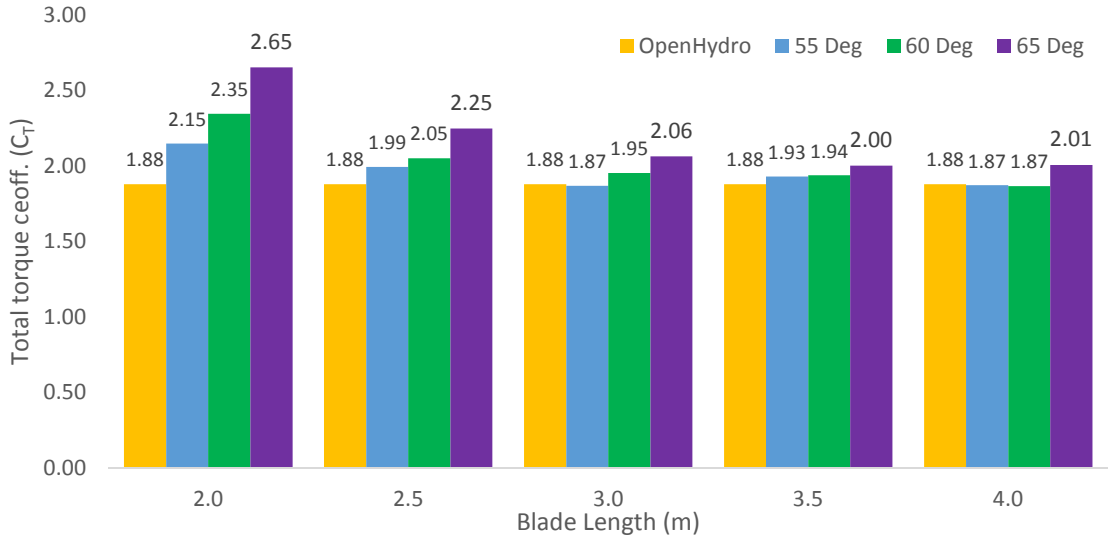

Figure 3.19. Total torque coefficient of the OpenHydro model compared to the 55º, 60º and 65º HELIOCHATT models

A study of the velocity and pressure contour plots is required in order to determine the design characteristics of the OpenHydro blade which have caused it to be less effective at generating torque than the larger twist angle classes of HELIOCHATT models. The first set of plots presented in Fig. 3.20 show the velocity and dynamic pressure contours, which illustrate a similar flow behaviour to that observed in the HELIOCHATT simulations. The same recirculation region is present near the rear surface of the blade, and a stagnation region also develops on the front surface. The flow velocity in both of these areas is low, which results in a low dynamic pressure. The attack angle that the OpenHydro blade makes with the incoming flow is aggressive enough to cause the recirculation region to become detached from the rear blade surface. This causes a high velocity counter flow to develop between the recirculation zone and rear surface, thus increasing the dynamic pressure on the rear surface. The stagnation region on the front surface of the blade also causes a low dynamic pressure to develop, which extends almost all the way from the leading to trailing edge of the blade. The length of the OpenHydro blade is not sufficient to cause a narrow passageway and a high velocity flow to develop, as was the case for the HELIOCHATT blades. Therefore the downstream portion of the front surface does not experience an increase in dynamic pressure, but instead is dominated by the low dynamic pressure caused by the stagnation region. The combination of high dynamic pressure on the rear surface and low dynamic pressure on the front surface results in a net negative dynamic torque.

The second set of plots in Fig. 3.20 show the static and total pressure contours, which also reveal similar flow patterns to those observed in the HELIOCHATT analysis. The stagnation region causes a high static pressure to develop on the front surface, and the recirculation region causes a low static pressure to develop on the rear surface. The large static pressure differential between the front and rear surfaces is the mechanism responsible for generating all the torque produced by the OpenHydro model, and in fact the negative dynamic pressure differential only detracts from the blade's effectiveness in this respect. These plots also illustrate how the flow behaviour around individual blades has much less of an impact on neighbouring blades, which is evidenced by the absence of interference with the front surface flow dynamics by the recirculation region of the next blade. This is due to the short blade length of the OpenHydro model, and the lack of blade overlap, as was illustrated in Fig. 3.3.

The third set of plots illustrate the turbulence behaviour of the flow, revealing a very similar profile to those observed in the HELIOCHATT simulations. Turbulence in the recirculation is again responsible for the decrease in dynamic and static pressure, and the magnitude of the turbulent region is comparable to the results from the 65^{o} class. It is also clear that the static and dynamic profiles combine to produce the total pressure profile, and all three can be linked through the turbulence profile.

An informed comparison can now be made between the conventional OpenHydro model and the new HELIOCHATT designs, based on both the total torque production and the flow dynamics around the blade surfaces discussed in the previous section. A quantitative analysis was presented in Fig. 3.19, which showed that with respect to total torque production, the OpenHydro model is surpassed by several of the HELIOCHATT blades from the largest twist angle classes. In fact the best performer from the HELIOCHATT series, the 2-m blade from the 65^{o} class, produced a total torque coefficient which is 30% greater than the OpenHydro blade. This would suggest that a significant potential exists for development of the HELIOCHATT design, especially those models which feature large twist angles. The qualitative analysis presented in the contour plots in Fig. 3.20 indicates that both the OpenHydro and HELIOCHATT blades seem to produce torque in the same general manner, and indeed feature flow dynamics which are quite similar. There is however a rather important difference in the magnitude of the dynamic torque produced; the negative dynamic torque produced by the OpenHydro blade is certainly a drawback, and an area in which almost all the HELIOCHATT blades perform better. This is therefore another motivation to further

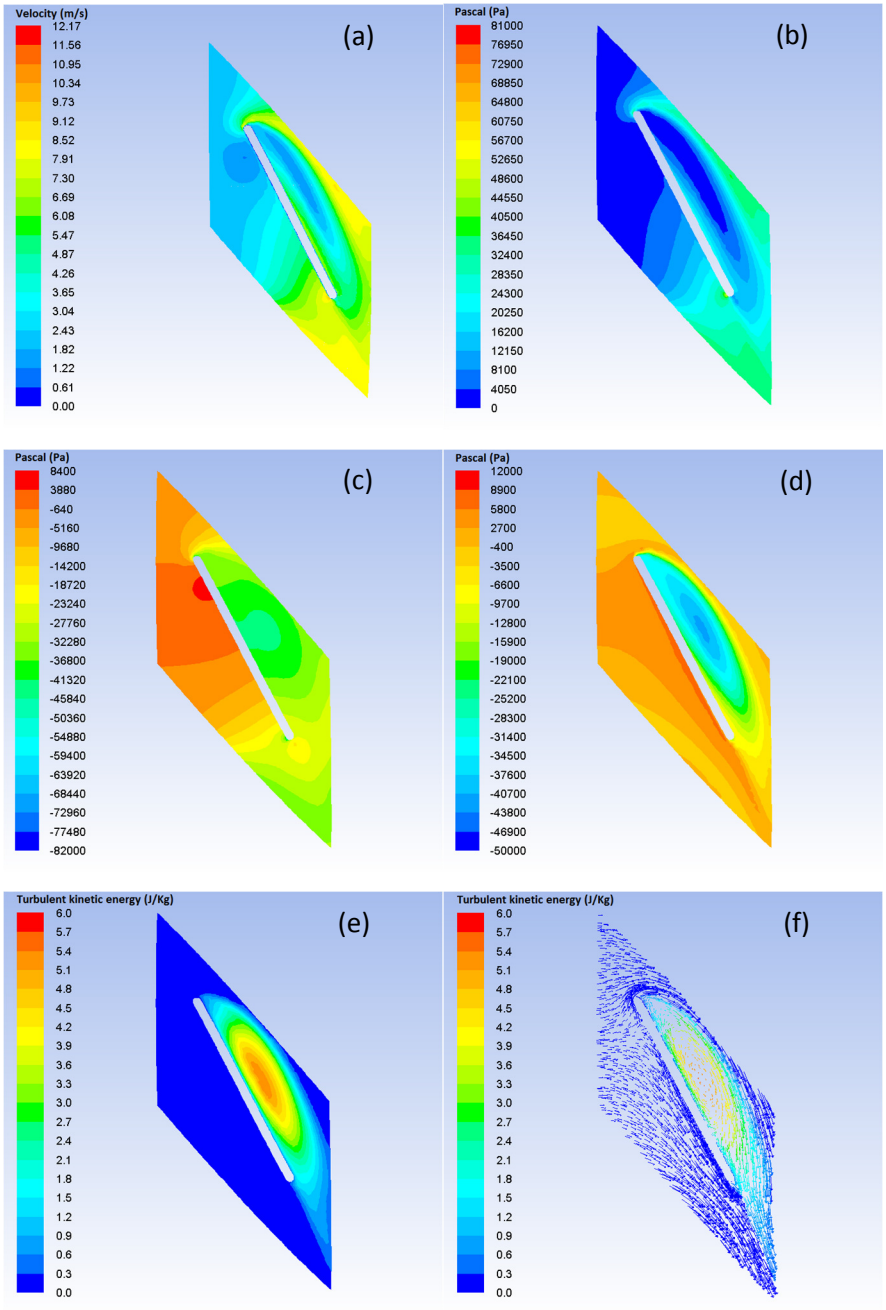

Figure 3.20. OpenHydro contour plots of a) velocity; b) dynamic pressure; c) static pressure; d) total pressure; e) turbulent kinetic energy; and f) velocity vectors

investigate the helical blade design, and perhaps capitalize on the high speed flow patterns which seem to be characteristic of this kind of blade.

3.3.5 Pressure Drop

The results thus far have been discussed exclusively with regards to the pressure and velocity profiles of the flow as it travels through the bladed section of the turbine, focusing on the near-blade regions. This provides insight into the specific mechanisms by which each blade geometry generates torque, identifying crucial design characteristics. This kind of analysis can be augmented by assessing the resulting pressure drop across the turbine rotor, thus providing an additional means by which to measure the amount of power extracted from flow. Conventional tidal turbines, not of the open-centre design, extract power from the flow by decreasing the velocity of the flow as it passes through the rotor section, which results in a negligible drop in pressure. Therefore in order to maintain continuity, the stream lines must expand as the flow leaves the rotor section. This places a limit on the amount of power that can be extracted from the flow, as the stream lines cannot expand indefinitely, and that limit is approximately 60% of the incident kinetic energy. It has been shown however, that ducted turbines can significantly exceed this limit, known as the Betz limit, as the geometry of the duct constrains the streamlines (Belloni, 2013). This causes a significant drop in pressure across the rotor section, thus altering the mechanism by which the turbine extracts energy. Therefore ducted turbines aim to maximize the pressure differential between the inlet and outlet of the turbine, which is achieved through duct geometry and blade design.

The open-centre turbine is inherently a ducted turbine, as the blades are fixed to the shroud at the tip, and the shroud itself extends from slightly upstream of the leading edge of the blade to slightly downstream of the trailing edge. The shroud then acts exactly as a duct, restricting radial flow and enhancing axial flow. Therefore the pressure differential between inlet and outlet is another parameter by which power extraction may be measured. For this reason the following section includes an assessment of the pressure drop across the rotor, and verification of the conclusions drawn about the blade geometry in the previous sections.

The plot in Fig. 3.21 presents the data regarding the total pressure differential from inlet to outlet for each class of blades. It is clear from this data that not only is there a very good correlation between twist angle and pressure drop, but also that the results agree exactly with the torque assessment presented previously. Indeed the 65^{o} class shows the most impressive pressure drop of all the classes, with the 2m blade showing the most dramatic differential of all. This is the same blade design which produced the most amount of torque, and the same twist angle class which was the overall best torque producing class.

The narrowing of the blade passageway was explained previously as acting like a nozzle, responsible for accelerating the flow through the bladed section. This mechanism is

also relevant here, where the blade design which features the narrowest of passageways also produces the greatest pressure drop. The effect of the passageway is further illustrated by this data, showing that as the blade length decreases and the passage narrows, the resulting increase in flow velocity causes a greater pressure differential to develop between the inlet and outlet.

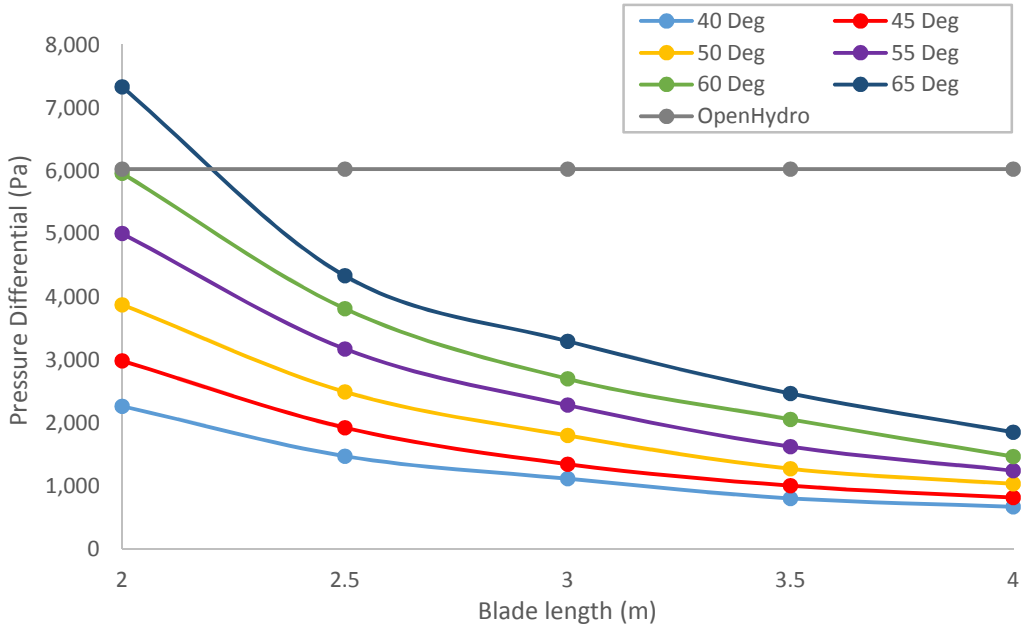

Figure 3.21. Pressure drop between inlet and outlet

It is important to note that the OpenHydro blade features a greater pressure drop than all but one of the HELIOCHATT blades, and yet it produces less torque than almost all of the largest three twist angle classes. This suggests that despite a large pressure drop, the OpenHydro model loses a significant amount of power through some other mechanism. It is most probable that this is due to a significantly smaller blade surface area, which is a result of the OpenHydro's short blade length and small circumferential dimension. As was shown in Fig. 3.3, a front view of the OpenHydro rotor reveals a negative overlap blade design, which means that instead of overlapping, the blades in fact do not cover the full frontal face of the turbine. The graph in Fig. 3.22 illustrates this disparity, showing that the total surface area of all 12 OpenHydro blades is less than the total surface area of all 8 HELIOCHATT blades, for all twist angle classes and all blade platoons. Therefore the OpenHydro design is able to overcome the challenge of a smaller surface area when in competition with the 40°, 45° and 50° classes, but is finally over taken by the 55° and 60° and 65° classes.

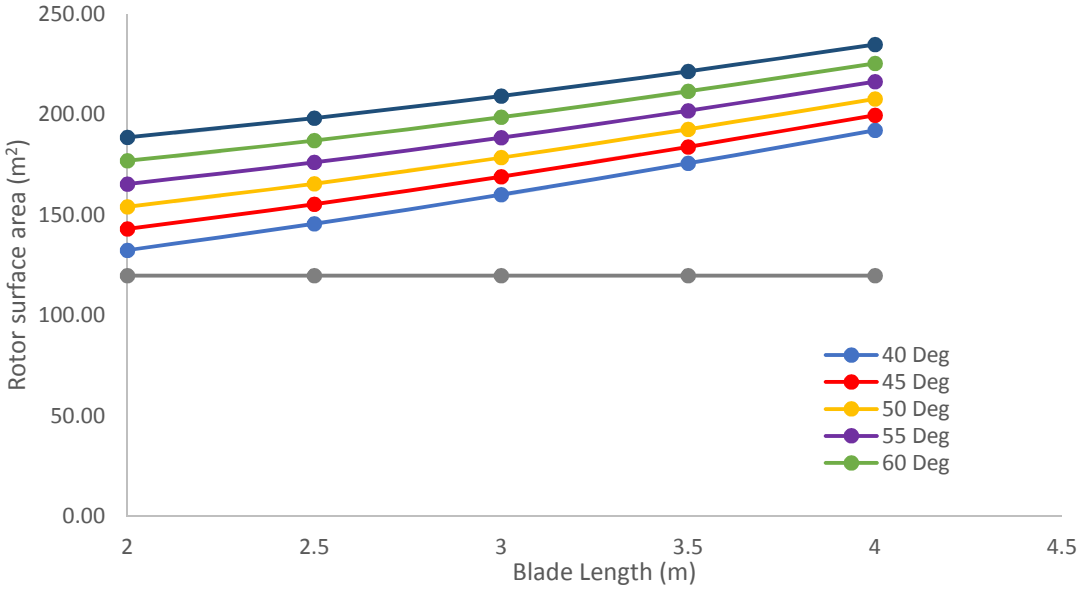

Figure 3.22. Total surface area of 8-bladed HELIOCHATT rotors and 12-bladed OpenHydro model

In summary, for the HELIOCHATT blades, the correlation between pressure drop and twist angle matches the correlation between torque production and twist angle. This indicates that the HELIOCHATT design is indeed reliant upon a large pressure drop between inlet and outlet in order to generate power. The OpenHydro model also produces a large pressure differential, which is in fact greater than all but one of the HELIOCHATT blades. However it produces less power than 50% of the HELIOCHATT designs due to a much smaller blade surface area. The superior torque performance of the HELIOCHATT blades, despite a smaller pressure drop, suggests that this design holds great promise, and provides additional grounds for developing the helical blade concept further.

Chapter 4

4. Conclusion and Future Work

The challenges associated with the harvesting of tidal energy have caused this source of renewable energy to remain largely undeveloped, despite an overabundance of potential. However, relatively recent advances in submerged technology have resulted in a rapid growth in the tidal energy sector in general, and specifically in the variety of tidal stream turbine designs in use and under development. The open-centre design is one such option, and it has been implemented by OpenHydro in a number of turbine designs which differ in scale and power generation potential. The method by which the OpenHydro models are scaled so as to vary the power output is through the enlargement of the outer diameter of the turbine, thereby increasing the lateral seabed footprint of the structure. This decreases the number of turbines that may be placed side by side in what is often a narrow tidal stream channel, which in turn decreases the net power production of the installation. Therefore it is the goal of this study to investigate the viability of a turbine design which may be scaled longitudinally instead of laterally, and which features helical blades as opposed to a flat conventional blade design.

A large number of design iterations were developed, varying in blade length and twist angle, and tested using a numerical approach. In an effort to perform an accurate assessment of the performance potential of each design without requiring a large amount of computation time, a unique CFD method was developed. The Fully Explicit stAtic Single Blade Model, referred to as the FEASiBLe model, facilitated a rapid testing process, and the results were extracted for all 30 blade designs. The performance of each blade was judged based on its ability to extract the maximum amount of power from the flow, and this was measured as the torque production potential. It is a pressure differential across the blade and the resulting pressure force which generates the torque, and so determination of the magnitude of the pressure differential is of prime importance. Each blade generates a static pressure differential as well as a dynamic pressure differential, and so the summation of the static and dynamic torque results in the calculation of the total torque potential. The new turbine design being investigated in this study is also compared to the performance of the conventional open-centre design employed by the OpenHydro model.

The blade geometries differ only in blade length and twist angle, and so the performance of each design is a function of these two parameters. It is crucial therefore to determine how variations in each affect the torque production of the blade, and if an optimum combination of

length and twist exists. From the results of this study several conclusions can certainly be drawn regarding the relationship between performance, blade length and twist angle.

4.1 The Effect of Twist Angle on Performance

The results are unambiguous regarding twist angle; an increase in twist angle leads to an increase in torque production, at any blade length. This is due to several reasons:

Increase of attack angle

If the blade length is held constant, the increase in twist angle results in an increase in attack angle. A larger attack angle produces a greater amount of flow recirculation behind the blade, as well as a more significant amount of flow stagnation on the upstream portion of the front blade surface. The low static pressure within the recirculation region and the high static pressure within the stagnation region generates a large static pressure differential across the blade, thereby leading to an increase in static torque. The opposite is true with respect to the dynamic pressure differential, which suffers in response to an increase in attack angle. This is due to the presence of a high velocity counter flow along the rear surface of the blade, which when paired with a relatively constant dynamic pressure along the front surface results in a weaker dynamic pressure differential overall.

Narrowing of passageway between blades

The increase in twist angle also leads to a narrowing of the passageway between blades, which results in an increase in the flow velocity through the passageway. The high velocity flow through the passageway impacts the downstream portion of the front blade surface, as well as the downstream portion of the rear blade surface on the same blade due to a ricochet action. The presence of the high velocity flow on the front surface of the blade leads to a high dynamic pressure, which is desirable for generating a large dynamic pressure differential. However on the rear blade surface the high velocity flow impinges on the low pressure recirculation zone, and therefore exposes the rear surface to a greater dynamic pressure. This adversely affects the dynamic pressure differential, which decreases the amount of dynamic torque production. Therefore blades with a narrower passageway generate less dynamic torque.

The static pressure differential is positively affected by a narrowing of the passageway, as this generates a high velocity and low static pressure on the rear surface of the blade, just downstream from the recirculation region. The result is essentially an extension of the low static pressure from the leading edge all the way to the trailing edge, by combining the effect

of the recirculation with that of the directed high velocity flow. In summary, the narrow passageway and accelerated flow cause an increase in static torque.

Increase in pressure drop

The narrowing of the passageway also has an effect on the pressure differential, which increases significantly with twist angle. This is due to the flow acceleration and the resulting difference in flow velocity between the inlet and outlet of the blade section. The ducted nature of the open-centre design is responsible for restricting the flow from traveling radially, and the blade passageway prevents tangential flow. Therefore the flow is forced to accelerate quite dramatically in order to maintain continuity, hence a large pressure drop between inlet and outlet develops.

4.2 Effect of Blade Length on Performance

The results regarding blade length are slightly less definitive, owing to a variation in the effect of blade length depending on twist angle. That is to say, the larger the twist angle the more sensitive the torque performance is to a variation in blade length. In fact the smaller twist angles show almost no deviation in total torque production across all blade lengths. Therefore the following observations regarding blade length pertain mostly to the three larger twist angle classes.

Decrease of attack angle

If the twist angle is held constant, then an increase in blade length leads to a decrease in attack angle. As was mentioned earlier, a large attack angle is important for generating low pressure flow recirculation and high pressure flow stagnation on the rear and front surfaces respectively. Clearly then an increase in blade length leading to a decrease in attack angle is not beneficial to the static pressure differential. Again, the dynamic pressure responds in the opposite manner, with the decrease in attack angle leading to an increase in dynamic torque. This occurs due to the reattachment of the recirculation region to the rear surface of the blade, thus exposing the rear surface to a low dynamic pressure. The high dynamic pressure on the front surface is largely unaffected by the decrease in attack angle, and so the result is an increase in the difference between front and rear dynamic pressure profiles.

The larger the twist angle the more important the blade length becomes, and in fact the largest twist angle class shows a rather dramatic decrease in torque of 25% between the 2-m and 4-m blades, whereas the smallest twist angle shows only a 10% decline. The reason for

this twist angle dependency with regards to blade length is not immediately obvious, and in fact it has not been determined to any sufficient degree of certainty. It is clear that a non-linear relationship exists between blade length and torque production for all twist angles, despite the fact that blade surface area and attack angle vary in a very close to linear manner. At this point, the results indicate that future studies should focus on the larger twist angles, and in doing so a better understanding of this relationship will undoubtedly be developed.

Broadening of passageway between blades

For any given twist angle, the increase in blade length leads to a broadening of the passageway between blades, which is the opposite result of increasing the twist angle. It should be noted however that an increase in blade length does not have the same effect as a decrease in twist angle, and this is due to the difference in the increments by which each is adjusted. This only shows that 5^{o} of twist does not correspond to 0.5 m of blade length, which is of course simply a matter of geometry, but is noted here merely to draw attention to the fact.

The impact of broadening the passage on the torque production is of greater consequence, and indeed it has the effect of decreasing the static and total torque. A broader passage facilitates a lower velocity flow, which is most influential on the rear surface of the blade. As it was the low static pressure on the rear surface which was responsible for generating the large static pressure differential, an increase in the rear static pressure necessarily leads to decrease in the static pressure differential. The total amount of torque generated by the blade is primarily a function of the static torque, and therefore the total torque follows suit and decreases as well.

Decrease in pressure drop

The effect of blade length on the pressure difference between inlet and outlet was explained previously as being a function of passage dimensions. Therefore the increase in blade length corresponds to an increase in passage width and a decrease in the pressure drop. What should be noted here however is that if the blade length increases, then the distance that the flow has to travel between inlet and outlet also increases. This means that the magnitude of the pressure drop decreases despite an increase in travel distance, which is perhaps counter intuitive if related to the pressure drop observed in pipe flow. The conclusion then is that the velocity of the flow is the most important variable with respect to the pressure drop between inlet and outlet.

4.3 Future Work

This study represents the first assessment of a helical blade open-centre horizontal axis tidal turbine, and as such it provides preliminary findings and highlights design iterations which hold promise. In the development of an original design concept such as this, it is usually necessary to carry out multiple studies of increasing detail and with a narrowing focus. The next phase of research will concentrate on the blade geometries which performed the best, and which deserve further investigation.

Moving mesh

For the present study, the decision to use a stationary blade and steady flow conditions was motivated by the need to perform a great number of simulations with limited calculation resources. This has proven to be a successful method for winnowing down the list of design candidates to a much smaller number of top performers. With a more manageable group of geometries to test, it is now possible to build a more sophisticated numerical model which will necessarily require an exponentially greater amount of time and computing power. The most significant upgrade is to incorporate a moving mesh, thus allowing for a more realistic simulation of the flow field around the blade. This makes it possible to resolve the effect of the turbine on the flow as well as the force applied by the flow on the turbine. In addition, the power generation potential can be calculated more accurately, using the rotational speed of the rotor and the resulting forces on the blades.

Larger flow field

The dimensions of the flow field used for this study were minimized in order to reduce the size of the mesh and the time required to resolve the flow. As it was only necessary to calculate the force applied to the blade surfaces, the flow through the open-centre and around the exterior of the shroud were not included in the simulation. These areas will need to be included in future studies if the true nature of the flow behaviour is to be determined, including wake effects and structural stresses. Therefore a much larger flow field is required, encompassing the entire turbine structure and extending 20-30 rotor diameters downstream.

Even with a larger flow field it is still possible to minimize the calculation cost with the use of periodic boundaries along planes of symmetry, however it would be beneficial to do so to a lesser degree than was carried out during the present study. This requires diving the domain into fewer sectors and perhaps containing two or three blades in each. Including more than one

blade in the domain increases the accuracy of the flow dynamics by directly simulating the interference between blade sectors, instead of assuming perfect symmetry across periodic faces.

Aerofoil geometry

Tidal turbines must be able to operate in a bi-directional flow by either reorienting the entire structure, altering the attack angle of the blade or by simply featuring an inherently bi-directional design. The HELIOCHATT is of the latter version, requiring neither reorientation nor blade adjustments when the flow direction of the tide changes. This means that the geometry of the blade must be such that it produces the same amount of power regardless of flow direction. Therefore future studies should also investigate the possibility of modifying the blade profile in a manner which maintains bi-directionality. Options include incorporating a variation in the blade width, modifying the leading and trailing edges and changing the angle that the blade makes with the hub and shroud.

Wake studies

The marine environments in which tidal turbines operate are sensitive to the destructive effects of wake turbulence, therefore any new design must also be assessed with regards to wake dynamics. This will involve using a make larger flow field extending up to 40 turbine diameters downstream. In addition, the wake interaction of multiple turbines placed in a fleet arrangement must be studied such that the efficiency of the installation does not suffer. A wake study of this nature will therefore be incorporated into the rotating mesh simulation, providing an accurate means to resolve the flow field behind a rotating turbine.

References

1. Oceans of energy (2009) European Ocean Energy Roadmap. Report commissioned by the European Ocean Energy Association

2. Lewis, A., Estefen, S., Huckerby, J., Musial, W., Pontes, T., Torres-Martinez, J., (2011) Ocean Energy. In IPCC Special Report on Renewable Energy Sources and Climate Change Mitigation, Cambridge University Press, Cambridge, UK and New York, NY, USA

3. Keenan, G., Sparling, C., Williams, H., Fortune, F., (2011) SeaGen Environmental Monitoring Programme Final Report. Commissioned by Marine Current Turbines, Ltd

4. Lloyd-Evans, L.P.M., (2005) A Study into the Prospects for Marine Biotechnology Development in the United Kingdom. Report Commissioned by the Foresight Marine Panel – Marine Biotechnology Group, Vol. 1

5. Polagye, B., Van Cleve, B., Copping, A., Kirkenhdall, K., (2010) Environmental Effects of Tidal Energy Development. Report Commissioned by the National Oceanic and Atmospheric Administration, NOAA Technical Memorandum NMFS F/SPO-116

6. OpenHydro Group Ltd., The Open-Centre Turbine. (http://www.openhydro.com/technology.html)

7. Sanderse, B., van der Pijl, S.P., Koren, B., (2011) Review of computational fluid dynamics for wind turbine wake aerodynamics. Wind Energy, Vol. 14, pp. 799-819

8. Masters, I., Malki, R., Williams, A., Croft, T., (2013) The influence of flow acceleration on tidal stream turbine wake dynamics: A numerical study using a coupled BEM-CFD model. Applied Mathematical Modelling, Vol. 37, pp. 7905-7918

9. Harrison, M.E., Batten, W.M.J., Myers, L.E., Bahaj, A.S., (2010) Comparison between CFD simulations and experiments for predicting the far wake of horizontal axis tidal turbines. IET Renewable Power Generation, Vol. 4, Iss. 6, pp. 613-627

10. Sorensen, J., Shen, W., (2002) Numerical modelling of wind turbine wakes. Journal of Fluid Mechanics, Vol. 124, pp. 393-399

11. Lee, J.H., Park, S., Kim, D.H., Rhee, S.H., Kim, M.C., (2012) Computational methods for performance analysis of horizontal axis tidal stream turbines. Applied Energy, Vol. 98, pp. 512-523

12. Masters, I., Willis, M.R., (2011) A robust blade element momentum theory model for tidal stream turbines including tip and hub loss corrections. Journal of Marine Engineering and Technology, Vol. 10. Iss. 1, pp. 25-35

13. Afgan, I., McNaughton, J., Rolfo, S., Apsley, D., Stallard, T. Stansby, P., (2013) Turbulent flow and loading on a tidal stream turbine by LES and RANS. International Journal of Heat and Fluid Flow, Vol. 43, pp. 96-108

14. Pope, S. B., (2000) Turbulent Flows. Cambridge University Press, UK

15. Wilcox, D. C., (1993) Turbulence Modelling for CF., DCW Industries, Inc.

16. Anderson, J. D., (1995) Computational Fluid Dynamics. The Basics with Applications. McGraw-Hill, Inc., La Canada, California, USA

17. Boussinesq, J., (1878) Essai sur la théorie des eaux courantes. Journal de mathématiques pures et appliquéees, 3e série 4, 335-376

18. Dewan, A., (2011) Tackling Turbulent Flows in Engineering. Springer, Inc., London, UK

19. Spalart, P.R., Allmaras, S.R., (1992) A one-equation turbulence model for aerodynamic flows. AIAA Paper (92-0439)

20. Menter, F.R., (1993) Zonal two-equation k-ω turbulence model for aerodynamic flows. AIAA Paper (1993-2906).

21. Fleming, C., McIntosh, S. Willden, R., (2012) Performance and Wake Structure of a Model Horizontal Axis Axial Flow Turbine. Technical Report RE-585, University of Oxford

22. ANSYS Inc. (2009a) ANSYS FLUENT 12.0 Theory Guide

23. Glauert, H., (1935) Airplane propellers, in W. Durand, Aerodynamic Theory, Vol. IV, Springer, Berlin

24. Belloni, C.S.K., Willden, R.H.J., (2011) Flow field and performance analysis of bidirectional and open-centre ducted tidal turbines. Proc. 9th European Wave and Tidal Energy Conference (EWTEC), Southampton, UK

Appendix A

A.1 The Blade Geometries

Twist Angle (deg)	Blade Length (m)	Helix Angle (deg)	Pitch (m)	Surface Area (m^2)
40	2	41.11	18.0	16.5
40	2.5	34.92	22.5	18.2
40	3	30.19	27.0	20.0
40	3.5	26.50	31.5	21.9
40	4	23.57	36.0	24.0
45	2	44.47	16.0	17.9
45	2.5	38.15	20.0	19.4
45	3	33.20	24.0	21.1
45	3.5	29.29	28.0	23.0
45	4	26.15	32.0	24.9
50	2	47.49	14.4	19.2
50	2.5	41.11	18.0	20.7
50	3	36.03	21.6	22.3
50	3.5	31.94	25.2	24.1
50	4	28.61	28.8	26.0
55	2	50.19	13.1	20.7
55	2.5	43.83	16.4	22.0
55	3	38.66	19.6	23.5
55	3.5	34.44	22.9	25.2
55	4	30.96	26.2	27.0
60	2	52.62	12.0	22.1
60	2.5	46.32	15.0	23.4
60	3	41.11	18.0	24.8
60	3.5	36.80	21.0	26.4
60	4	33.20	24.0	28.2
65	2	54.81	11.1	23.6
65	2.5	48.60	13.8	24.8
65	3	43.39	16.6	26.1
65	3.5	39.02	19.4	27.7
65	4	35.34	22.2	29.3